LAPPEENRANTA-LAHTI UNIVERSITY OF TECHNOLOGY (LUT)

School of Engineering Science

Master Degree program in Chemical Engineering for Water Treatment

Daryna Ihnatiuk

SUNLIGHT-DRIVEN PHOTOCATALYTIC REDUCTION OF NOBLE METALS IONS TO NANOPARTICES

Examiners: Assoc. Prof. Eveliina Repo

Assoc. Prof. Teodora Retegan

ABSTRACT

Lappeenranta-Lahti University of Technology LUT

School of Engineering Science

Master Degree program in Chemical Engineering for Water Treatment

Daryna Ihnatiuk

Sunlight-driven photocatalytic reduction of noble metals ions to nanoparticles

Master's thesis

2019

67 pages, 30 figures, 9 tables

Examiners: Assoc. Prof. Eveliina Repo, Assoc. Prof. Teodora Retegan

Keywords: PHOTOCATALYSIS, PHOTOREDUCTION, VISIBLE LIGHT IRRADIATION, GRAPHITIC CARBON NITRIDE, GOLD, PLATINUM, NANOPARTICLE

The investigation of the noble metal ions photoreduction to nanoparticles was conducted in this Master Thesis. Four types of graphitic carbon nitride powders were synthesized through the thermal polycondensation reaction of four different precursors (melamine, dicyandiamide, urea and melamine-cyanuric complex). The chemical and physical properties of synthesized materials were studied by XRD, SEM, TEM, EDS, UV-VIS spectroscopy, BET and BJH methods. Photocatalytic properties of the samples were tested in the photoreduction of Au^{3+} and Pt^{4+} to Au and Pt-nanoparticles from tetrachloroauric and hexachloroplatinic acids aqueous solutions, respectively. Ethanol and water were used as the hole scavengers. DRS and UV-VIS spectroscopy were applied for the reaction efficiency control in solid and liquid phases of the experiments, respectively. The analysis of the thermodynamic parameters of the process, experiment conditions development, experimental data interpretation and correlation of those to the materials' parameters were conducted and future directions of the research in related area were proposed.

ACKNOWLEDGEMENTS

I would like to thank my thesis advisor Assoc. Prof. Eveliina Repo of the School of Engineering Science at Lappeenranta-Lahti University of Technology for her support, trust and help on this research conduction.

Also, I would like to give many thanks to my supervisor PhD Oksana Linnik from Chuiko Institute of Surface Chemistry at National Academy of Sciences of Ukraine, who has shared her knowledge and energy during many years of my professional growth till now and has held my hand on the each step of the way.

I would also like to thank to my supervisors MSc Camilla Tossi, Prof. Ilkka Tittonen and whole MQS group of the Department of Electronics and Nanoengineering at Aalto University for the opportunities they provided me with for the experiments and for support and patience during my endless experiments in the lab.

Finally, I would like to thank to my parents, boyfriend and friends, who supported me on this way, continuously encouraged me during my studies as well as thesis writing and have believed in me sometimes even more, than I did. I do appreciate that a lot.

Daryna V. Ihnatiuk

TABLE OF CONTENTS

LIST OF SYMBOLS AND ABBREVIATIONS

λ (lambda) – wavelength, nm

θ (theta) – angle of X-rays in X-ray diffraction, degree

BET method – Branauer-Emmet-Teller model for specific surface area measurements

BJH method - Barrett-Joyner-Halenda method for pore volume measurement

CB – conduction band

CNT – carbon nanotube (SWNT – single wall CNT, MWNT – multi wall CNT)

DCDA – Dicyandiamide

DMSO – Dimethyl sulfoxide

DRS – Diffuse Reflectance Spectrometry

EDS – Energy-dispersive X-ray spectroscopy

g-C_3N_4 – graphitic carbon nitride

MCA – Melamine-cyanuric acid complex

NHE – normal hydrogen electrode

PV – pore volume

REE – Rear Earth Elements

SEM – Scanning Electron Microscopy

SPR – Surface Plasmon Resonance

SSA – Specific Surface Area

HR-TEM – High Resolution Transmission Electron Microscopy

UV-VIS – Ultraviolet-Visible light

VB – valence band

WEEE – waste of electrical and electronic equipment

XRD – X-ray diffraction

1 INTRODUCTION

During the last century, incredible transformations in areas of technology, industry and social attitude in general have happened. On one hand, the extraordinary and accelerating development of the technologies in electronics and electrical equipment is bringing new goods to the customer in both everyday home and working life, pampering people with new devices being engineered, produced and sold daily. On the other, the development of new social and economic strategies of product life cycle intensification, goods realization and focusing on consumption has affected objectives, tendencies and behavior of mankind in the market relations and causes overconsumption of the products and services, when chasing after the fashion and prestige.

At the same time, such a large market request makes manufacturers of the products increase their production capacities and consumption of the raw materials. In a new era of electronic and electrical devices, different expensive, precious and rare earth chemical elements (REE) are used as the important components. Their mining is stressful for both industry and ecosystems, as far as their content in the ores is extremely low in most cases, and new technologies for such ores processing and their waste products treatment after the mining have to be applied. Traditional pyrometallurgy means are arguably inefficient in this case, when hydrometallurgy could be efficient, but quite hazardous, due to the use of acids and bases for the metals leaching from the ores. On the other end of the product life chain, the significant, emerging and complicated problem of electrical and electronic equipment waste (WEEE) treatment appears. This group of waste is hazardous for the environment and contains substantial amounts of Critical Raw Materials and precious metals that exceed their concentrations in the raw ores. Thus, recovery and recycling of scarce resources from WEEE is reasonable and of high importance for the sustainable development and circular economy targets implementation. (European Commission, 2019; Directive EC, 2012)

However, even leaching of the REEs and precious metals from the WEEE with hydrometallurgy is not a complete solution of the problem, due to the high cost and complicated separation of these elements from the mixed leachates. Traditional methods would either be inefficient, expensive or environmentally unfriendly.

From the variety of new developing methods for metals recovery, photocatalysis should be noted. It is a process of chemical reaction intensification by the synergic effect of catalyst and irradiation involvement (Khan et al., 2017). Photocatalysis brings an opportunity

for safe recovery of REE and precious metals and meets ideas of sustainable development and circular economy. Investigations in this area have been very intensive during last decades, due to the positive environmental effects and possibility of low energy consumption at high efficiency of the process (Khan et al., 2017; Zhou et al., 2016; Ghosh, 2018). Recently, new materials for visible light-induced photocatalysis have been studied, in order to make industrial application of the process both less challenging and more profitable.

Despite the high scientific interest towards photocatalysis application for different chemical processes like organic pollutants degradation, water splitting and CO_2 reduction, the photoreduction of noble metals has been studied relatively less, due to the complicated and conditions-demanding process (Grzelczak and Liz-Marzan (2014)). (Zhou et al., 2016; Wang et al., 2012) Papers that report photoreduction of noble metal ions to nanoparticles, usually, have been performed in "pure" conditions of single ingredient solutions, although, while of interest for practical application, noble metals have to be recovered selectively from mixed solution of waste leachate. Polymeric materials like graphitic carbon nitride ($g\text{-}C_3N_4$) are worth investigating for this specific task. This material has been reported in various in last ten years (Zhou et al., 2016; Wang et al., 2012; Zhang et al., 2017), but rarely for the aforementioned application.

The aim of this study is to investigate noble metals photoreduction with help of visible light-active photocatalysts from the WEEE that is richer on that element, than primary ore, especially from the perspective of future industrial application of this method. Moreover, potentially sunlight-induced photocatalysis is economically viable, when the request for an environmentally friendly method development and improvement already exists in framework of strategies of sustainable development and circular economy.

In scope of this Master Thesis, synthesis and characterization of the photocatalysts have been performed. Photocatalytic properties of the samples have been studied on photoreduction of noble metals ions to nanoparticles. For proper conclusions of the study to be made, analysis of experiments and correlation of those to material parameters have been done. The thesis is arranged in two parts: theoretical background (literature review) on relevant topic and experimental part with description of the experiment conditions, results and their discussion, on basis of which conclusions are made. References are listed at the end of the document.

2 THEORETICAL BACKGROUND

2.1 Photocatalysis

As mentioned above, photocatalysis is a catalytically intensified light-induced process. Intense photocatalytic processes investigation has started after the process of photocatalytic water splitting under UV-irradiation has been proven by Fujishima and Honda in 1972 (Fujishima and Honda, 1972).

The concept of the process is based on semiconductors and their specific properties. In solid state physics, all the materials are classified by their energy levels structure as conductors, insulators and semiconductors (fig. 2.1). Each material has its own molecular orbitals structure, due to the element-specific amount of valent electrons on the external electron layer and their energy. When the atoms of the material are excited, electrons from the valence band – in other words, valence orbitals – tend to transfer to– the common energy field in the bulk of the material called the conduction band.

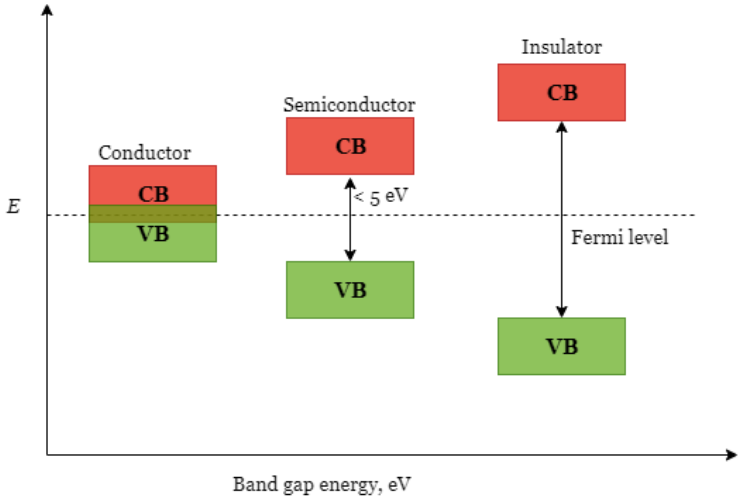

Figure 2.1. Energy levels of conductor, semiconductor and insulator

Thus, in conductors these bands are overlapped and the valence electrons are easily moved in the energy region that extends across the Brillouin zone that in normal conditions doesn't have electrons. For insulators, energy gap between the valence electron excitation to the conduction state is so high that only the very high energy influences could cause the electron transition through the bandgap. For semiconductors the electron transition is allowed and it has a discrete number of allowed energy states, meaning that electron transfer is possible with some quants of certain energy being added to the system. This charge separation

is limited in time and ends up with electron back transfer for the ground state establishment, although the lifetime of charge carriers' separation is sufficient for different reactions to proceed. (Ghosh, 2018; van de Krol and Grätzel, 2012)

Van de Krol and Grätzel (2012) state that the electron transition between the valence and conduction bands could go in two pathways (fig. 2.2): for the direct transition of the electrons stimulation the photon energy is enough to excite the valence band orbitals; when for the indirect the process is also assisted by the phonon of specific energy $h\omega$ (lattice vibration). This is explained by the highest position of the valence band and the lowest position of the conduction band of the material and, if they have the different atomic geometry of the lattice, the change in crystal momentum is required for such transition, which basically is not sufficient from the photon.

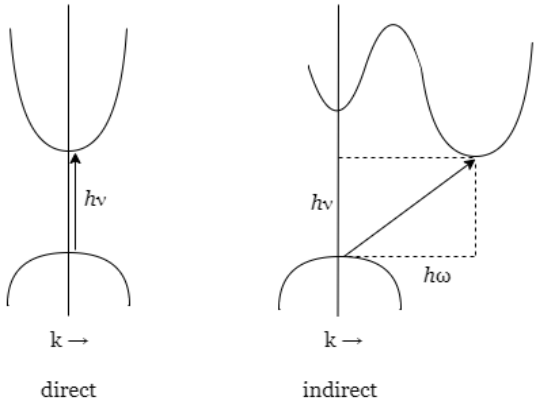

Figure 2.2. Direct and indirect bandgap electron transitions in semiconductors

The structure of the valence and conduction bands of semiconductors (fig.2.3) allows the sensitization of the reduction-oxidation reactions through the radicalization mechanism.

Photocatalytic reactions are dependent on the energy of the incident electromagnetic irradiation or, in other words, they are wavelength dependent and traditionally these reactions are grouped as UV, UV-VIS- or visible light-induced processes. The photons of equal or higher energy than the bandgap energy between the valence band (VB) and conduction band (CB) of the semiconductor, are absorbed by the photocatalyst's particles and are capable of excitation resulting in transferring of the electrons from the VB to the CB. The electrons, when leaving the VB, leave the non-compensated charge – called a hole – which is capable of oxidation of the electron-donor molecule. When water molecules act as donor, hydroxyl radicals are produced. At the conduction band, oxygen dissolved in solution reacts with photogenerated electron and a superoxide radical is formed. Both hydroxyl and superoxide

radicals are used for the reduction-oxidation reactions intensification. (Fujishima et al., 2000; Hagen 2006; Khan et al., 2015)

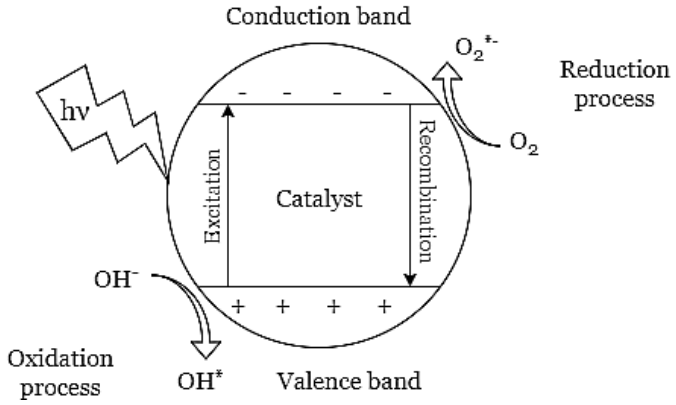

Figure 2.3. Schematic photocatalytic processes

However, generated electron-hole pairs are also able to participate directly in oxidation or reduction of different species, if those are adsorbed on catalyst's surface. Kisch (2013) summarized the mechanisms steps in the following equations (2.1-2.3):

$$SC \overset{h\nu}{\rightarrow} SC(e_r^-, h_r^+) \tag{2.1}$$

$$SC(e_r^-, h_r^+) \overset{h\nu}{\rightarrow} SC + h\nu/heat \tag{2.2}$$

$$SC(e_r^-, h_r^+) + A + D \rightarrow SC + A^{\cdot -} + D^{\cdot +} \tag{2.3}$$

where

D is electron donor,

A is electron acceptor,

SC is semiconductor.

An undesired reaction of the mechanism, namely recombination of the charges (eq. 2.2) is favored at the point of system relaxation and efficient back electron transfer prevents redox reactions completion (eq. 2.4 – 2.6):

$$A^{\cdot -} \rightarrow A_{red} \tag{2.4}$$

$$D^{\cdot +} \rightarrow D_{ox} \tag{2.5}$$

$$D^{\cdot +} + A^{\cdot -} \rightarrow A + D \tag{2.6}$$

Recombination or annihilation of the charge carriers by each other is an important factor in photocatalysis and it could proceed under different pathways (Zhang and Yates, 2012). Defects of the structure and impurities in the semiconductor cause the formation of different “trap states” (fig. 2.4) for the photogenerated electron-hole pairs, which would limit the redox reactions efficiency.

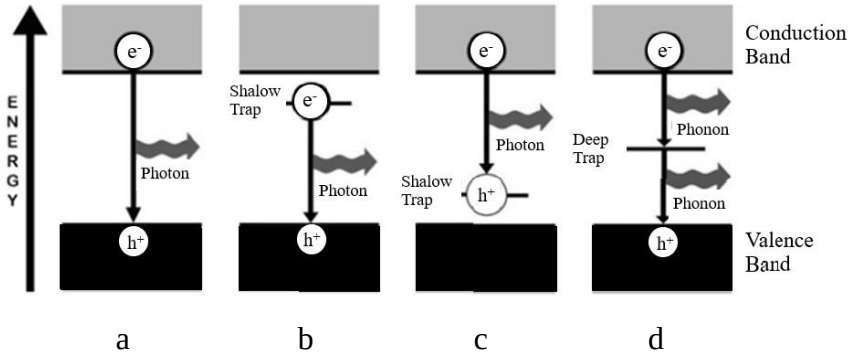

Figure 2.4. The recombination pathways of a photogenerated electron−hole pair. a) Band-to-band radiative recombination; b) electron-trap state to valence band; c) conduction band to hole-trap state; d) non-radiative recombination via an intermediate state (adapted from Khan et al., 2017)

Recombination of the charge carriers could go through the radiative and non-radiative pathways. For indirect bandgap electrons transition materials like TiO_2, recombination process goes through the non-radiative way and results in heat being released. It has been proved (Mendive et al., 2012) that the energy, released through recombination, leads to the destruction of the catalyst’s surface.

According to the type of photocatalyst, involved into the process, photocatalysis can be homogeneous or heterogeneous (Fujishima et al. 2000). Homogeneous photocatalysis typically involves transition metal complexes for generation of hydroxyl radicals under the photon or thermal excitation, which are used afterwards for organic compounds degradation. Heterogeneous photocatalysis suggests excitation of solid phase system like TiO_2, ZnO, SnO_2 and has proved to be superior, due to low cost, ambient conditions requirement and less waste formation (Khan et al., 2017).

Due to complicated process mechanism, different parameters could affect the photocatalysis efficiency. (Fujishima et al., 2000; Khan et al., 2015)

Semiconductor particle size, structure and shape are important parameters for the photocatalyst performance. The crystallinity of the material plays the key role for its semiconductive and photocatalytic properties. The size of the crystallites affects the specific surface area (SSA), available for the process, and, as far as process is interfacial, the amount of active sites participating in the process. It is a well-known fact in photocatalysis research that TiO_2 has three different phases: anatase, rutile and brookite. For many years anatase has been claimed the superior one, which would yield in higher surface area and better process performance, however, recently debates on rutile better performance have started, due to its better crystallites shape, which would help to decrease the recombination rate of the charges (Dong et al.(2017)).

Additionally, temperature and pH of the process also bring their effect. Generally, in photocatalysis on TiO_2 samples the efficiency of the process is decreased with the temperature growth, due to the higher recombination rate and desorption of the reactants (Malato et al., 2009; Rajeshwar et al., 2008). On the other hand, activation energy of the process increases significantly at temperatures lower than 20 ^{o}C. At the same point, pH affects the surface charge of the material a lot and makes different reactions favorable, due to adsorption – desorption equilibria on the reactive interface (Reza et al., 2015; Neppolian et al., 2002).

Light intensity directly affects the process efficiency because it relies on the amount of photons being absorbed by the material. However, excessive irradiation causes increase in recombination rate and, thus, decreases whole process efficiency. (Reza et al., 2015; Malato et al., 2009)

The amount of catalyst has controversial effect. Till the optimum point it accelerates the process, due to more radicals formed. But, on the other hand, higher catalyst loading makes it more complicated for the light to pass through the whole reaction volume and, at some point, particles begin to scatter more light than absorb. (Malato et al., 2009; Rajeshwar et al., 2008)

The concentration of the target compound has a relative effect to the catalyst loading: at extremely low concentrations process kinetics are limited because of rare interaction between the targeted compound and the catalyst; at the concentrations above the optimal operation window some compounds are getting stabilized and, consequently, products are formed more slowly. (Reza et al., 2015; Malato et al., 2009; Rajeshwar et al., 2008)

Attractive prospects of low energy and chemicals-consuming technology that would serve multi-purpose tasks (Fujishima et al., 2000; Rajeshwar et al., 2008; Khan et al., 2017) have promoted a lot of scientific work in the area since 1972 (Zhou et al., 2016; Wang et al., 2012; Zhang et al., 2017) and the studies have been mainly focused on two tasks: new materials preparation, testing and improvement of their parameters. New materials that have been studied could be separated by their nature on the metal-based and non-metallic materials and both these classes still could undergo modification procedures (fig.2.5).

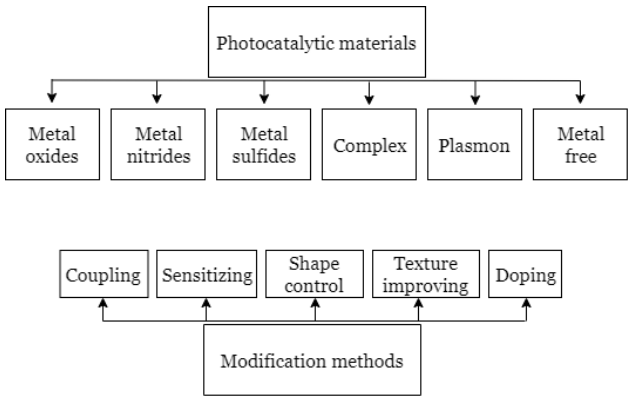

Figure 2.5. Development of different photocatalysts

Modification approaches could be classified into: coupling of different catalyst groups or sensitization with dyes, texture or shape improvement, doping with metal or non-metals and bandgap engineering by building different sublevels. The first method suggests a combination of two separate bandgap systems for the charge separation improvement. Texture or shape improvement aims the change of structural and crystallinity properties of the material. However, all these modifications may be applied to the various compounds studied as a separate and single active component. (Zhou et al., 2016, Khan et al., 2017; Wang Y. et al., 2012)

2.1.1 Metallic systems

Metal-based photocatalysts are represented by oxides, nitrides and sulfides of the d-block metals. They have a modest bandgap energy (up to 3.8 eV, fig. 2.6) (Khan et al., 2015) and some of them (TiO_2, ZnO) have proved to be efficient photocatalysts under UV-irradiation or even visible light (sulfides), but the latter ones also would go under photocorrosion and toxic leachates would get released to the solution (Van Dijken et al., 1997; Iwashina et al., 2015; Liang et al., 2015).

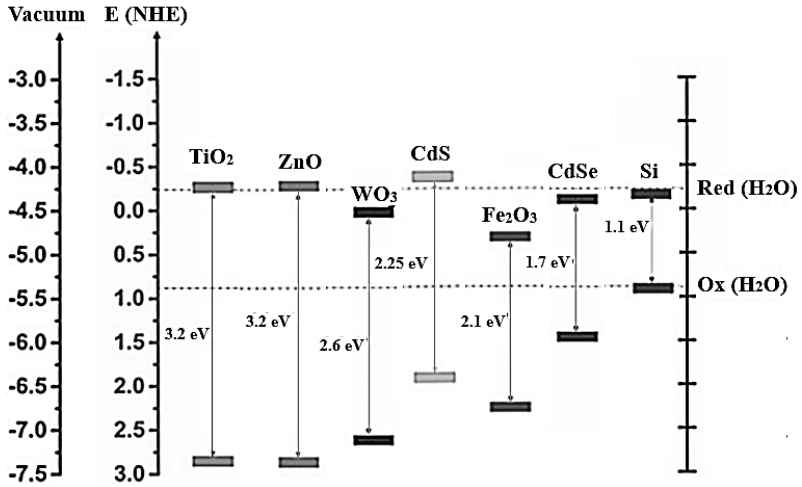

Figure 2.6. Bandgaps and redox potentials, using the normal hydrogen electrode (NHE) as a reference for several semiconductors (adapted from Khan et al., 2017)

Oxides

Titanium dioxide (TiO_2) has been proven to be the most efficient photocatalyst among the other metal oxides. The most photocatalysis tendencies, effects and parameters have been established with it (Bickley et al., 1973; Butler and Davis, 1993; Carey et al., 1976; Fujishima and Honda, 1972; Inoue et al., 1979; Yamagata et al., 1988), making it the most extensively studied metal oxide in terms of photocatalysis. It has three different crystallinity forms: anatase, rutile and brookite. Anatase has been reported multiple times as the one with the highest photocatalytic activity, high SSA, but also higher rate of defects. Multiple modification attempts have been made on characteristics improvement of TiO_2 and, initially, d-block metals have been used as dopants for bandgap manipulation (Zhou et al., 2016). Doping of TiO_2 with nitrogen and other different heteroatoms has also been investigated (Ihnatiuk et al., 2017).

ZnO has also been reported as an efficient catalyst (even with a better performance than TiO_2) with a bandgap energy around 3.3 eV. However, it was considered unstable, owing to photocorrosion (Zhou et al., 2016). Thus, different modification strategies have been applied to improve the material activity and stability: doping with different metals (Pawinrat et al., 2009; Ullah and Dutta, 2008) and non-metals (Rehman et al., 2009), coupling of semiconductors (Uddin et al., 2012).

A variety of other metal oxides, such as Ga_2O_3, Fe_2O_3, Cu_2O, WO_3, have been intensively studied as alternatives for TiO_2 and ZnO (Zhou et al., 2016).

Complex metal systems

Complex metal systems have been developed as an approach for band structure engineering, by means of different metals ions introduction to the photocatalyst structure and have shown good photocatalytic efficiencies, despite high cost of their components when REEs, In, Ta, W, Ge, V, or Mo have been used (Anpo and Thomas, 2006; Liu et al., 2010; Tang et al., 2004; Tang et al., 2003; Zou et al., 2001).

Metal sulfides and nitrides

The non-oxide group of photocatalysts possesses more electronegative potentials, due to the valence bands of S 3p and N 2p orbitals compared to the O 2p orbital. ZnS and CdS are the most studied representatives of this group and, especially, ZnS. Even with a bandgap energy of 3.6 eV, it has shown high efficiency in photocatalytic processes, due to fast generation of the charge carriers in the processes of CO_2 reduction and hydrogen evolution (Hu et al., 2005; Fujiwara et al., 1998). CdS, on the other hand, is capable of visible light absorption (bandgap energy is near 2.4 eV) (Bao et al., 2008) and multiple efforts on in solving the photocorrosion issue have been tried on it, mostly through material hybridization (Hamity et al., 2008; Yu et al., 2014).

Noble metal-based plasmonic photocatalysts

Photocatalytic properties of noble metals nanoparticles have been studied in regard to their excitation under visible light, due to surface plasmon resonance. They have been studied as dopants for TiO_2, in order to red-shift the absorbance spectrum of the photocatalyst. This phenomenon has promoted the study of the photocatalytic mechanism of such system and high charge separation was explained by the transition of the electrons from nanoparticles to the CB of TiO_2. For this aim Au and Ag nanoparticles have been investigated (An et al., 2010; Chen et al., 2008; Tian and Tatsuma, 2005).

2.1.2 Non-metallic systems

As an alternative to metal-based photocatalytic systems, various carbonaceous materials have been studied (Choi et al., 2010; Leary and Westwood, 2011; Parket al., 2010; Tajima et al., 2011; Zhang et al., 2010). Carbon-based materials with an organized structure act as a possible future substitute for metal-based photocatalytic systems, due to the high abundance of this element on Earth and to the semiconductive nature of its structure. These materials also

bring an opportunity for cheap visible light-driven photocatalysis and are known to be good hole-conducting materials (Khan et al., 2017), which could be a suitable solution of problem regarding metal photocorrosion during the photocatalytic process (Zhou et al., 2016).

Development of polymeric carbonaceous materials has been considered as a promising way, due to their porous structure, controllable synthesis and various modification options of both structure and surface (Zhou et al., 2016; Khan et al., 2017; Martin, 2015). Nowadays, some stable allotropic forms of carbon, namely, graphite, graphene, fullerenes and their modifications are extensively studied. Recently, as a promising photocatalyst, graphitic carbon nitride has been widely investigated (Dong et al., 2013; Du et al., 2012; Fan et al., 2015; Hong et al., 2014; Liang et al., 2015b; Liu et al., 2016a,b,c; Shi et al., 2015; Wang et al., 2009; Xing et al., 2014; Yang et al., 2013).

Graphene has been reported as a promising material for photocatalytic nanocomposites development. It has a planar layered graphitic structure with π-network and extraordinary electrical properties (Li et al., 2011) with fast classic carrier transitions. Oxygen functionalization of graphene sheets brings a disturbance to its sp^2-hybridized 2-dimensional structure and transforms the orbitals of carbon atoms into sp^3-hybridized forms, which later act as transport barriers for carriers (Johns and Hersam, 2013). This makes graphene oxide a hybrid material with easily adjustable bandgap and oxidation-reduction properties, suitable for various photocatalytic applications (Matsumoto et al., 2016). Graphene also has been studied in combination with TiO_2, making the photocatalytic nanocomposite efficient for high speed electron transfer from CB of TiO_2 (Dong et al., 2013; Zhao et al., 2016). As a cheaper analog of graphene, graphitic carbon nitride has also been studied.

Carbon-based nanocomposite C_{60}-fullerene enables oxidation of organic compounds and has exhibited decent antibacterial and antiviral properties by visible light-induced formation of the singlet oxygen ($^1O_2$) (Arbogast et al., 1991; Choi et al., 2010; Yamakoshi et al., 2003). In hybrid material C_{60} with TiO_2, an effective bandgap shift to the visible light region with both hole and electron being involved in photocatalytic studies has been reported (Zhang et al. 2016a, b).

Carbon nanotubes (CNTs) are, ideally, perfect graphene planes rolled into cylinders and fixed by two semifullerene units (Serp et al., 2003). They improve photocatalytic properties of different composites, when incorporated to the structure. CNTs cause multiple changes in the composite: the augmentation of the amount and quality of active sites, the elimination of the

charge carriers recombination and, naturally, the bandgap modification (Dai et al., 2009; Kang et al., 2007; Leary and Westwood, 2011; Tryba, 2008; Yao et al., 2014).

Carbon quantum dots (CQDs) are new nanocrystalline or even amorphous (due to their size less than 10 nm) quasi-spherical nanoparticles of graphitic carbon or graphene oxide with diamond-like sp^3-hybridized defects that possess high electron transfer ability and have enhanced the activity of photocatalytic composites. (Di et al.2015a, b)

2.2 Graphitic carbon nitride (g-C_3N_4)

The aim of this study was to consider and investigate a photocatalyst for industrially viable photocatalytic reduction of noble metal ions to nanoparticles. The suggested photocatalytic material had to meet several requirements:

- to be able to absorb visible light irradiation;
- appropriate CB and VB potentials positions;
- the cheap and simple synthesis procedure;
- non-toxic and robust material;
- corrosion and photocorrosion resistant;
- flexible towards its properties adjustment.

Graphitic carbon nitride (g-C_3N_4) was considered as a suitable material that fulfilled all the mentioned above requirements. It is a stable and robust polymer with a graphene-like layered structure and semiconductive properties. It has demonstrated a crystalline structure with bandgap energy of 2.7 eV and, hence, intrinsic light absorption takes place in visible spectral range (420 – 600 nm). Thus, it has been studied for a variety of catalytic and photocatalytic reactions, and its activity towards water splitting, organic compounds transformation, CO_2 reduction and environmental photocatalysis has been proven (Low et al., 2015; Luo et al., 2016; Ong et al., 2016; Xu et al., 2016).

Graphitic carbon nitride is one of the first synthesized polymers that have been reported (Liebig, 1834) and it has been known for almost 200 years. However, intensive research on g-C_3N_4 photocatalysis has started only in the last decade (Dong et al., 2013; Du et al., 2012; Fan et al., 2015; Hong et al., 2014; Liang et al., 2015b; Liu et al., 2016a,b,c; Shi et al., 2015; Wang et al., 2009; Xing et al., 2014; Yang et al., 2013).

Different polymeric precursors of carbon nitride have been debated since the XIX century (fig. 2.7). The ideal C_3N_4 crystalline phase has not been condensed, despite numerous attempts, and the ones of high crystallinity still were rare and unclear. Moreover, the ideal crystals are not of high interest in this case, due to the high catalytic performance of the material with a sufficient amount of defects. However, the understanding of the polymerization stages would cause the coupling with different structures and development of controlled structures easier. (Wang et al., 2012)

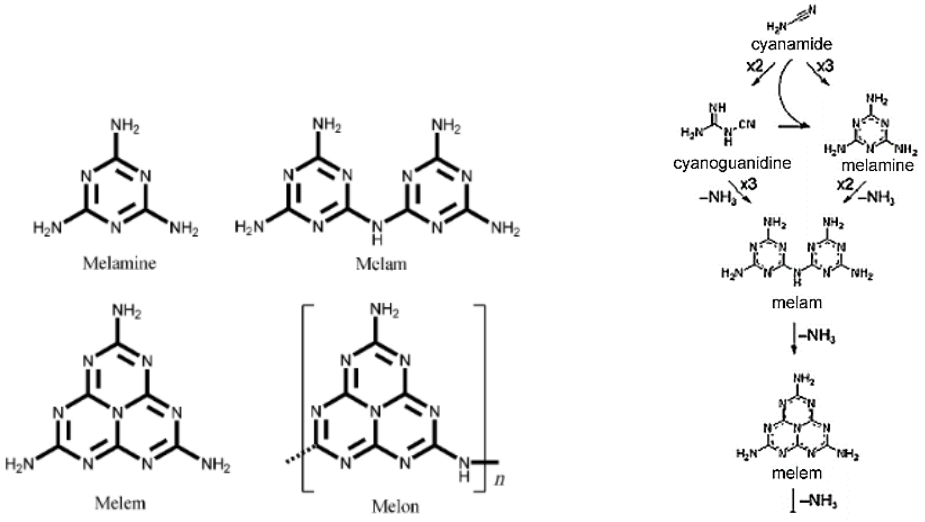

a b

Figure 2.7. Carbon nitride structural precursors (a) and condensation reactions of cyanamide to form carbon nitride (b) suggested by Liebig (adapted from Wang et al., 2012)

For now, structure of g-C_3N_4 is described as a planar π-conjugated molecular network similar to graphene layers with distance of 0.326 nm between the layers bonded by means of van der Waals forces. It consists of heptazine tri-s-triazine (C_6N_7, also referred to as melon) blocks, built of C, N and H (fig. 2.8). (Khan et al., 2017)

Wang et al. (2012) have mentioned two different modifications of g-C_3N_4 (s-triazine and tri-s-triazine) and stated that tri-s-triazine unit has been found to be energetically favored and more stable. Wang et al. (2015) have synthesized and compared the photocatalytic performance of both modifications. Mesoporous tri-s-triazine sample has been proven to be the most active, exhibiting higher crystallinity and larger surface area as well as a hierarchical porous structure that would affect all the critical factors of photocatalytic processes (charge separation, abundance of active sites, pathway of the photogenerated charge carriers from BG to the surface of the photocatalyst and their trapping). Such difference could also be explained

by the synthesis methods of these two forms: the higher degree of polymer condensation was obtained through the thermal treatment, than through the low temperature liquid phase reaction.

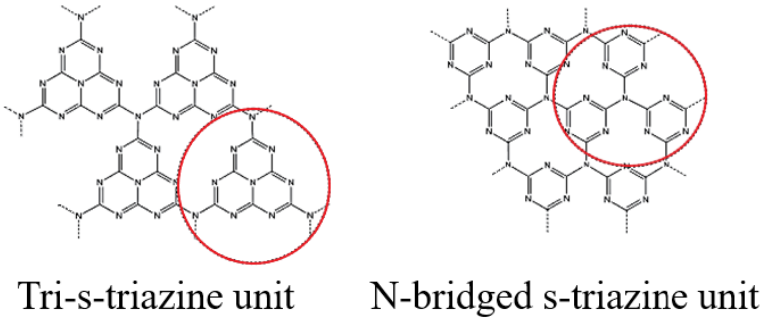

Figure 2.8. Structure scheme of g-C_3N_4 with N-bridged tri-s-triazine and s-triazine as building blocks

Tri-s-triazine or heptazine modification has been reported to be stable at heating up to 600 ^oC, due to high degree of condensation and presence of the covalent bonds in the lattice. Moreover, g-C_3N_4 has been reported as one of the most heat-resistant organic polymers in general and total decomposition of the material was observed only at 750 ^oC. From the point of view of chemical stability, it withstands interaction with different acids, alkali and is insoluble in most solvents, owing to the stacking of the layers and van der Waals interaction between separate layers. (Wang et al., 2012)

However, the material has been studied mostly in powder form, due to the low mechanical strength related also to highly open structure of the material (Sun et al., 2016).

2.2.1 Optical and photocatalytic properties of g-C_3N_4

The analysis of different studies related to g-C_3N_4 has revealed the information about material properties variation when different synthesis techniques are applied. Synthesis conditions, precursors used, pre- and post-treatment strategies highly affect the final product and its characteristics, namely, light absorption edge, C/N ratio, specific surface area, porosity and polymer structure that has a significant influence on the material photocatalytic performance (Wang et al., 2012).

Graphitic carbon nitride has been reported as a middle-bandgap (around 2.7 eV) semiconductor with indirect electron transition by p – p orbitals. Thus, it is capable of visible

light absorption with the peak at 420 – 460 nm of the visible light part of the spectrum, what is approved also by the yellow color of the material itself. Khan et al. (2017) defines g-C_3N_4 as a multifunctional catalyst. Presence of π-conjugated system combined with terminal -NH and -NH_2 groups stipulates electronic or nucleophilic properties, ability to form hydrogen bond and to show photocatalytic activity simultaneously. Considering g-C_3N_4 photocatalysis, it is known that nitrogen atoms act as oxidation sites, while carbon atoms behave as the reduction ones. On the other hand, Martin (2015) suggested the crucial effect of tertiary nitrogen atoms linking the heptazine units on g-C_3N_4 activity.

The XRD pattern of graphitic carbon nitride points on two characteristic peaks: the intense narrow 2θ peak at 27.4^o which corresponds to (002) plane of graphitic materials and interlayer stacking peak signed for aromatic materials. Distance between the layers is suggested to be 3.26 Å. The small 2θ peak at 13.22^o corresponds to the structural packing motif of (100) plane. (Wang et al., 2015, Zhou et al., 2016)

The low photocatalytic activity of bulk carbon nitride samples has driven the investigation of possible modification and bandgap engineering of the material. Numerous attempts have been done on material characteristics improvement and have resulted in their significant development. Currently, few excellent reviews on this topic have been published and those are summarized in Table 2.1. (Zhou et al., 2016)

Different precursors for g-C_3N_4 polycondensation, such as cyanamide, dicyandiamide (DCDA), thiourea, and urea have been reported (Martin, 2015). Wang et al. (2015) discussed the different modifications of carbon nitride preparation through two different routes. The material synthesized by thermal treatment of melamine was superior in photocatalytic activity with respect to the one from low temperature reaction and the authors relate that to higher condensation rate of the former sample. Further, highly ordered hollow carbon nitride structures synthesized from melamine–cyanuric acid complex with improved photocatalytic activity have been obtained (Shalom et al., 2013).

Chemical functionalization is an efficient method of material characteristics control, so far doping of the material with different heteroatoms has been studied. Traditionally, it is being done in two ways: tailoring of the surface after the synthesis or in-situ functionalization during the synthesis procedure. (Wang et al., 2012)

Table 2.1. Literature reviews on g-C_3N_4 modification and investigation

Author	Year	Details
Wang et al.	2012	- band structure manipulation through doping and copolymerization - approaches for porous structures development - material parameters evaluation (photochemical water splitting, organic oxidation and dehydrogenation reactions)
Zheng et al.	2012	- perspective on the synthesis of controllable structures and morphologies, - future for environmental remediation, energy conversion and storage.
Zhu et al.	2014	- synthesis of g-C_3N_4 - application for NO decomposition, differentiating oxygen activation sites, - nanomaterial synthesis.
Zheng et al.	2015	- synthesis and modification of tailored g-C_3N_4 for water splitting - electronic structure modulation - nanostructure design - crystal-structure engineering - heterostructure construction
Dong and Cheng	2015	- different exfoliation strategies for the synthesis of 2D g-C_3N_4 nanosheets (thermal oxidation, ultrasonic, chemical exfoliation)
Ong et al.	2016	- design and synthesis of g-C3N4-based materials, - analysis of physiochemical properties on the basis of DFT calculations (band structure, optical and electronic properties and separation of charges of the hybrid photocatalysts) - applications and the future in water splitting and CO_2 reduction and environmental remediation
Cao et al.	2015	- design and synthesis of g-C_3N_4-based photocatalysts (pristine g-C_3N_4 and semiconductor composites for bandgap engineering) - photocatalysis by carbon materials - different cocatalysts - Z-scheme heterojunctions.

Various carbonaceous p-conjugated/polymeric materials, owing to their unique electron and hole-transporting nature, high conductivity, suitable redox potential and stability in oxidized state, are compatible to form surface junctions to increase separation of electron–hole pairs. They help to improve utilization of the solar spectra by extending the optical absorption towards the visible region. The pyridinic-N atoms act as active sites of the photocatalyst, due to the delocalized p-electrons favoring the adsorption of O_2 molecules. The types of materials that could form hybrid materials with graphitic carbon nitride and their influence on final material properties have been summarized in Table 2.2. However, many of those are quite expensive and their introduction to the material structure was suggested to be unpractical. (Khan et al., 2017)

Yang et al. (2015) discussed the ideas of the structural modification of graphitic carbon nitride by templating with soft (surfactants and block copolymers, ionic liquids, and gas bubbles) or hard templates (silica, anodic alumina oxide, carbon) or biotemplates. It helps to increase SSA of the bulk material and improve the material structure. This aspect of modification will be discussed in more details in the following section.

Table 2.2. Coupling of g-C_3N_4 with different p-conjugated materials and polymers and their effect on material photocatalytic performance (Khan et al., 2017)

Material	Effect
Graphene	large contact area for charge transfer across the interface is formed
CNT	morphology and structure control; light absorption capacity enhancement; acts as an acceptor of photogenerated electrons; increases the efficiency of charge separation
Fullerenes (C_{60})	favours reduction reaction; an excellent electron acceptor to retard charge recombination
Polyaniline (PANI)	improves photoresponse in visible part of the spectrum; possesses good stability, non-toxicity, corrosion protection and efficient electron–hole transportation ability; good hole acceptor under visible irradiation
Poly-3-hexylthiophene (P3HT)	possesses high hole mobility; reduction of the electron–hole recombination process caused by distribution of electrons
7,7,8,8-Tetracyanoquinodimethane (TCNQ)	possesses a highly conjugated system; charge transfer complexes formation, due to strong p–p stacking interaction; rapid and efficient charge carriers separation
Polyacrylonitrile (PAN)	improved separation of charge carriers under the visible light irradiation; effective electron channelization

2.2.2 Synthesis of g-C3N4

Many synthesis techniques have been used for graphitic carbon nitride polycondensation with different precursors and additives. By now various synthesis schemes are categorized onto three main approaches (fig. 2.9) based on the treatment procedure and template used.

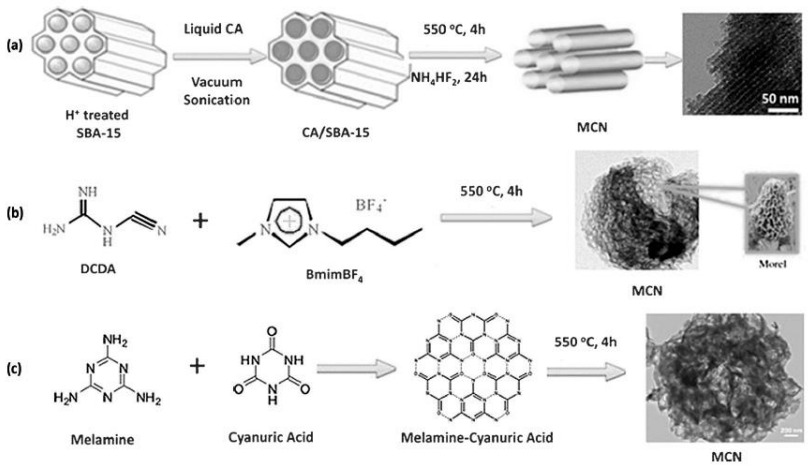

Figure 2.9. Different synthesis approaches: (a) nanocoating, (b) soft-templating and (c) self-assembly (adapted from Zhang et al., 2017)

Nanocoating

Hard templating or nanocoating is a synthesis approach that involves the addition of different templates to the synthesis process in order to improve materials SSA (which is, usually, not higher than 10 m^2 g^{-1} for the bulk) and structural features. This approach mainly suggests utilization of the solid templates based on silica, taking into account their inert nature. Typical representatives of these solid templates are silica beads SBA-15. After the synthesis process, these hard templates would still be present in the volume of the material. Thus, different fluoride-based solutions (NH_4HF_2 or 5–10%-w HF) have to be used for template removal. The area could get increased after nanocasting procedure up to two orders of magnitude with respect to the bulk one. (Wang et al., 2012)

As a carbon source typically cyanamide is used, when different additives for higher nitrogen content also may be applied. This method is quite time consuming and synthesis procedure could take up to weeks. It shows advantages of controllable and flexible synthesis with the precise strategy and, when being most studied, it also brings disadvantage of long procedure time. Moreover, it always involves hazardous fluoride-containing reagents into the synthesis and, thus is undesirable for the industrial application. (Zhou et al., 2016)

Soft-templating

As far as nanocoating (nanocasting) is dangerous and does not show any future opportunity for its real application, more safe methods had to be developed. The “greener” and relatively faster method of soft templating has been investigated recently. (Yang et al., 2015)

This method involves soft templates on polymer basis mixing with the precursor prior to the thermal treatment. During the thermal treatment, the holding sequences are introduced to the process, so that soft template polymer could boil and evaporate slowly and leave pores in the material volume afterwards. These soft templates are the polymers of inert nature and, typically, are the amphiphilic block polymers like Pluronic F127, P123, F68. Except those, imidazolium-based ionic liquids (ILs) are favorable choice and, if amphiphilic block polymers would result in the blocked or dead pores, ILs would produce nanoporous structures with good porosity and enormously high SSA. (Wang et al., 2012; Lee et al., 2009; Lee et al., 2010)

However, lack of understanding of the interactions between soft templates and precursor molecules, lack of systematic studies of various ILs for synthesis and final sample

properties, make the process less controllable and clear, therefore more research in this area would be required. Another drawback of this method is lack of information about the ionic liquids and their relatively high price, limit their application on industrial scale.

Self-assembly

This approach involves hydrogen-bonding during the synthesis process through direct, specific and reversible interaction that helps to form ramified structures and non-covalently bonded stable aggregates through a spontaneous molecular association in equilibrium conditions, without any soft or hard templates involvement (Shalom et al., 2013).

Cyanamide and its derivatives could be used as the precursors since they can be a source of both carbon and nitrogen and, in turn, the evaporated gases would be applied as the volume and pore increasing agent. In case of self-assembly, synthesis proceeds quite fast with high degree of condensation.

This method is considered an easy and inexpensive method for graphitic carbon nitride preparation. The other benefit of the self-assembly procedure is the fact that its materials have been studied for the photocatalytic activity more than the materials obtained by the other methods. However, this method is restricted by the choice of starting mixtures, as far as not all of the precursors can form hydrogen bonding and lower SSA of the synthesized materials is noted.

As an important statement, it should be mentioned that the studies with different synthesis approaches combination have been met frequently. Some of them and, mostly, the ones related to the self-assembly are mentioned in the Table 2.3 below.

Table 2.3. Analysis of different interesting cases of g-C3N4 synthesis

Reference	Synthesis description	Reactants	T, ^{o}C	Time (h)	SSA (m^2g^{-1})	C/N	Performance test	Result
Jun et al (2013)	MCN with a hollow spherical morphology	melamine cyanuric acid dimethyl sulfoxide	550	15h	77	0.72	RhB degradation	95% degraded in 1 h
Shalom et al (2013)	Cyanuric acid-melamine complex calcination	melamine Chloroform Ethanol Water cyanuric acid	550	15h	45	0.7	RhB degradation	100% degraded in 105 min
Liang et al (2915)	3D porous g-CN monolith (PCNM) by thermal polymerization of melamine sponge (MS) filled with urea	Melamine sponge Urea	550	24-48h	78	0.75	HER	29.0 μmol h−1
Zhang et al. (2014c)	porous graphitic carbon nitride (pg-C3N4) materials have been prepared by pyrolysis of dicyandiamide in air using urea as bubble template	DCDA Urea HNO3 0.1M	530	23h	60		Phenol and MB dergadation under VIS	phenol decomposition was 0.039 h−1
Shi et al. (2015)	Porous graphitic carbon nitride (pg-C3N4) was prepared through in situ bubble templates such as (NH4)2S2O8	(NH4)2S2O8 melamine	25-2h- 50-5h- 550-2h	15h	6.4 to 55.0	0.64-0.65	RhB and phenol degradation; HER	RhB DD: 96% in 40 min; Phenol degr: 55%HER: 35-100 umol/h
Wang et al (2015)	Tri-s-triazine	Melamine Pluronic F68 H2SO4 Lithium nitride Cyanuric chloride Diglyme	600 190	22h 36h	2.5-185.4	0.68-1.00	HER	1520 umol h-1 g-1
He et al. (2015)	a facile sulfur-bubble template-mediated synthesis of uniform porous g-C3N4 through the thermal condensation	Melamine Sublimed sulfur	600	4h	29-46	0.695	HER; RhB degradation	50 umol h-1 92%RhB degraded in 50 min
Han et al (2016)	Atomically thin mp nanomesh of g-C3N4 by solvothermal exfoliation of mp g-C3N4	Dicyandiamide Isopropanol (IPA)	600	3d	331	0.83	HER	490 umol h-1-g at 550nm
She et al (2016)	Post-treatment by mixture of inorganic acids of g-C3N4 synthesized by condensation at 550	Melamine Ethanol H2SO4 and HNO3	550	26h	109.3		HER; MO degradation	189.3 umol h-1 60%MO degraded in 3.5h
Fang et al (2015)	Nitrogen self-doped g-C3N4 was synthesized using melamine pretreated to provide additional nitrogen with further heat treatment in air	Melamine Hydrazine hydrate	550	28h	9.21	0.59	HER	44.28 umol h-1
Zhou et al (2016)	direct polymerization of citric acid with urea	Urea Citric acid	550	9h	85-92	0.6	HER	63.7 umol h-1

2.2.3 Application of g-C_3N_4 in photocatalysis

Water splitting

From a theoretical point of view, graphitic carbon nitride is capable of hydrogen fuel production by water splitting under visible light, without any co-catalysts or sacrificial electron donor or acceptor addition. The electronic structure of the g-C_3N_4 allows oxygen or hydrogen evolution and its bandgap is sufficient to overcome the endothermic potential of water splitting. (Wang et al., 2012)

However, on practice it requires at least minimal augmentation of co-catalyst like Pt to give a rise to the process. A lot of investigations have been done in this area and plenty of successful modifications have been published (Zhou et al., 2016; Martin, 2015), although the highest results still do not exceed 4%, what is still inappropriate for practical applications (Martin, 2015). Either doping with fluorine or nitrogen or mesoporosity integration would help to increase the reduction processes efficiency, while sulfur-doping and dye sensitization would enhance oxidation.

Degradation of organics

Graphitic carbon nitride has been studied for different organic substances degradation through the photocatalysis. This process has the advantage of harmless and efficient transformation of pollutants into easily degradable subproducts or even makes complete degradation to CO_2 and H_2O possible. As such pollutants, different substances are considered: pharmaceuticals, dyes, personal care products and emerging contaminants. (Wang et al., 2015)

2.3 Noble metals photoreduction

Nowadays, noble metals and REEs are of high interest for the industry: they have found wide application in many modern technologies and, especially, electronics. However, the abundance of these elements on the Earth is low and consequently their recovery and recycling are required. During the WEEE treatment, metals are leached from the circuit boards by the acids and mixed metal leachate has to be treated further for components separation and purification.

Formation of nanoparticles would open opportunities of higher efficiencies in the separation of metals for recovery process. Grzelczak and Liz-Marzan (2014) have discussed

the driving energy sources for the nanoparticles formation process and electromagnetic irradiation was considered as the promising energy source with tunable and controllable parameters. Radiolysis was found interesting, due to the uniform reducing agent formation, however, its high energy input limits its use. UV-irradiation was reported in many different papers, as far as it led to dissociation of transition metal ions into colloidal form under the irradiation. The photolysis of $HAuCl_4$ with formation of Au-nanoparticles has been observed under irradiation at 254 nm. Different polymers and additives could be used for the stabilization of synthesized nanoparticles. In case of visible and infrared-irradiation, utilization of the nanoparticles with the localized surface plasmon resonance for formation of the new nanoparticles would make the process work efficiently.

Photocatalysis has been rarely applied for noble metals photoreduction aiming for their recovery, whereas the modification of different photocatalytic materials with metal nanoparticles doping (Badhwar et al., 2013; Lu et al., 2015; Quintana et al., 2010; Wang et al., 2013) or the synthesis of plasmonic photocatalysts as mentioned in section 2.1.1 have been discussed more.

Photochemical synthesis of noble metals nanoparticles as co-catalysts has been reported to be performed under both UV and VIS-irradiation as well as different seeding materials (metal oxides or carbonaceous materials) could have been applied for this task (Grzelczak and Liz-Marzan (2014)).

Only a few studies on the recovery of noble metals by photocatalytic reduction could be found. Guo et al. (2014) reported recovery of Au on g-C_3N_4 under visible light irradiation in the inert atmosphere with high recovery rates. The reduction was selective and efficient, however, authors did not discuss the use of any hole scavenger that could intensify and improve the process.

3 EXPERIMENTAL PART

3.1 Research materials and methods

3.1.1 Materials

Materials used were of analytical grade: melamine (Aldrich), dicyandiamide (DCDA) (Aldrich), cyanuric acid (VWR), urea, ethanol, 99.5% (Aldrich) and dimethyl sulfoxide (DMSO) (Aldrich). In the experiments deionized water was used.

3.1.2 Synthesis description

For g-C_3N_4 synthesis four different precursors have been used to study different material structures with different characteristics towards metal photoreduction:

1) Melamine;
2) DCDA;
3) Urea;
4) Melamine-cyanuric acid complex (MCA).

In order to make synthesized materials comparable between themselves, they went through the same thermal treatment procedure. Synthesis scheme was considered on the basis of the literature reviewed in section 2.2.2 and would look as following for all the bulk samples of g-C_3N_4: 5.0 g of Melamine/DCDA/Urea were placed in the ceramic crucible with the perforated aluminum foil on the top and were baked up to 550 ^oC for 4h and at 550 ^oC for 4h in the tube CVD furnace. After the polycondensation procedure materials were allowed to cool down naturally in the tube to the ambient temperature.

In case of MCA-sample, complex had to be prepared previously. Thus, 1 g of melamine was dissolved in 40 mL DMSO, 1.02 g of cyanuric acid was dissolved in 20 mL of DMSO (stirred for 1 hour). After that, the solutions were mixed for 15 min together to form white precipitates. Later, precipitate was filtered, washed with ethanol and dried in oven at 50-60 ^oC for 2 hours. Then, the complex was baked in a furnace (OTF-1200X, MTI Corporation) under the same conditions as described above for all the other materials.

Yield of the product was calculated with the following formula (eq.3.1):

$$Y = \frac{m_{product}}{m_{initial}} \cdot 100\% \quad (3.1)$$

3.1.3 Characterization

Synthesized materials properties were studied with various techniques to collect data about both surface and structural features of the samples, so that the following material activity and efficiency in the process of metals photoreduction could be compared with or explained by the material's parameters. Surface and optical properties of the samples were studied with scanning electron microscopy, N_2 adsorption/desorption technique, BET and BJH models fitting as well as ultraviolet-visible light diffuse reflectance spectroscopy. Structural properties were tested with high resolution transmission electron microscopy, energy-dispersive X-ray spectroscopy and X-ray diffraction. Photocatalytic activity of the material was checked in the photoreduction reaction of noble metals ions to noble metals nanoparticles. Metal ions concentration in the solution was measured with ultraviolet-visible light spectroscopy, while nanoparticles growth on the surface of powder was monitored by visible light diffuse reflectance spectroscopy.

Scanning Electron Microscopy (SEM)

This method is widely used in research routine nowadays. Main principle of the method is based on the interaction of the high energy electrons beam with the sample surface. The electrons emitted by a high-voltage gun hit the surface of the sample and either get backscattered or diffractely backscattered or cause secondary electrons emission. All those electrons are captured by detectors and recorded for conversion into the image with a high depth of field.

SEM imaging for g-C_3N_4 was done with the Field Emission SEM JEOL JSM-6335F (Japan) at 15.0 kV with the secondary electrons detected. To prevent charging, samples were fixed on conductive tape and covered with 60 nm of Chromium by the Chromium sputterer K575X from Emitech.

Specific surface area (SSA) measurement with Brunauer-Emmett-Teller (BET) method and Barrett-Joyner-Halenda (BJH) method for pore volume and distribution

Both methods are based on calculations of adsorption/desorption isotherms data of N_2 gas on the surface of the material. The physisorption on the surface occurs due to the Van der Waal's interactions and is an extension from the Langmuir monolayer adsorption model to the multilayer theory. BET method is helpful in specific surface area measurement based on the volume of gas being adsorbed and the mass of material studied, when BJH method allows calculation of the pore size and pore distribution from the desorption isotherms for the porous materials.

For the thesis both methods were applied to detect the surface area and the porosity of synthesized materials. Nitrogen gas adsorption and desorption were performed on the Microtrac BEL BELsorp Mini II.

X-ray diffraction (XRD)

XRD is used to determine the atomic and molecular structure of a crystalline materials. The X-rays hit the material surface and undergo the elastic scattering. Parameters of the materials are in dependence to the angles of coherent and incoherent scattering and are related through the Bragg's law (eq. 3.2):

$$n\lambda = 2d \sin\theta \tag{3.2}$$

where

n is integer,

λ is the wavelength of irradiation,

d is the spacing between the atomic planes

θ is the angle between the X-ray angles and the atomic planes of the material.

The diffraction pattern was obtained by measurement of intensity change when the angles of X-ray source and detector were varied from 5 to 60 deg with the speed of 10 deg min^{-1} at Rigaku SmartLab X-ray diffractometer. Also, glass reference had to be subtracted from the samples diffraction patterns in order to eliminate any influence on the material properties measurement.

High resolution Transmission Electron Microscopy (HR-TEM)

TEM is applied for the imaging of relatively small particles, by transmission of a high voltage electron beam through the sample and these electrons refraction around the atoms of

the lattice. Sample is prepared by drop-casting on a copper grid (with a carbon film underneath for relatively small particles that could fell into the grid holes). TEM allows measurement of non-conductive materials without damaging them (unlike SEM), so no specific material pretreatment would be required.

HR-TEM JEOL JEM 2800 (Japan) was used for both the characterization of the synthesized polymer powder grain structure and characterization of the nanoparticles formed during the photoreduction process.

Energy-dispersive X-ray spectroscopy (EDS)

Energy Dispersive Spectrometer as an additional detector of HR-TEM JEM 2800 was used for the qualitative and quantitative study of the material parameters, such as C/N ratio, and to verify nanoparticles formation during the photoreduction experiments. The main principle is based on the measurement of the X-rays emitted from the material's surface, when electrons from the materials surface are stimulated by the TEM electron beam. The energy of these X-rays is element specific and allows their recognition. This analysis suggests not only surface atoms characterization, but makes possible the investigation of up to 1 μm depth of the sample.

Ultraviolet-Visible light Diffuse Reflectance Spectroscopy (UV-VIS DRS)

The interactions between the electromagnetic light and solid materials could be described by three phenomena: absorption, transmission and reflection and their relation is described by following equation:

$$1 = A + T + R \tag{3.3}$$

where

A is absorbance,

T is transmittance,

R is reflectance.

The light absorption is a crucial parameter in photocatalysis, since it gives information about the materials ability to absorb light of specific wavelenght and, thus, the bandgap energy of the specific substance. Semiconductive materials have only discrete bands for the

electrons allowed states and probability and character of the electrons transition (direct or indirect) are calculated with the Tauc relation (eq. 3.4):

$$(\alpha h\nu) = A(h\nu - E_{BG})^n \tag{3.4}$$

where

α is absorption coefficient,

$h\nu$ is the energy of the irradiation,

A is the constant, based on the effective masses of the holes and electrons

n is a parameter which is equal $\frac{1}{2}$ for direct or 2 for indirect transitions.

The absorption coefficient can be calculated from the reflectance value in the Kulbeca-Mulk relation (eq. 3.5):

$$\alpha = \frac{(1-R)^2}{2R} \tag{3.5}$$

In the framework of this study, the diffuse reflectance spectra (DRS) of the synthesized powders were measured with spectrometer, integration sphere and light source from Ocean Optics (fig.3.1). For the reflectance-transmittance-absorption relation T was suggested to be 0, due to the adequate thickness of the measured layer. Thus, absorbance of the material could be calculated as (eq. 3.6):

$$A = 1 - R \tag{3.6}$$

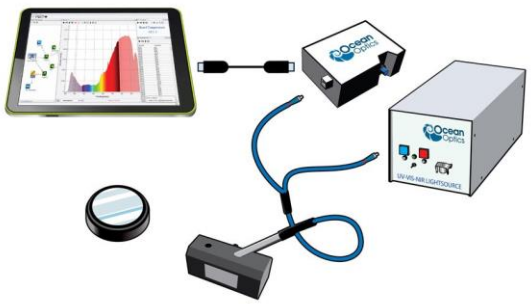

Figure 3.1. The DRS measurement setup (Oceanoptics.com, 2019)

UV-VIS Spectroscopy

This method is widely used for the measurement of the optical density of the liquids that correlates to the concentration of the ions and molecules dissolved in the liquid phase. It estimates the difference in ability to absorb the light of specific wavelengths between the

reference sample and the measured sample. The correlation between the light intensity transmitted by the liquid corresponds to the concentration of studied substance and is described by the Beer-Lambert law (eq.3.7):

$$A = \frac{1}{T} = -\log\left(\frac{I-I_b}{I_o-I_b}\right), \tag{3.7}$$

where

A is absorbance in arbitrary units,

I is the intensity of the light passing through the studied sample,

I_b is noize measured when the light beam is blocked,

I_o is initial light intensity passing through the reference.

For the light absorbance measurement the equipment from Ocean Optics was used (fig.3.2) and consisted of a Deuterium-Tungsten light source, cuvette holder, spectrometer and optical fibers to deliver the incident light to the detector through the cuvette.

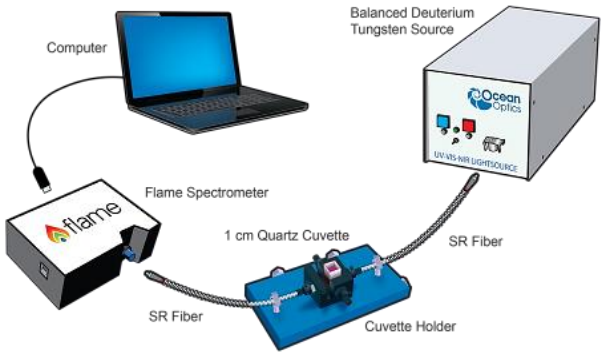

Figure 3.2. Ocean Optics spectrometer unit for the light absorption measurement of liquid phase (Oceanoptics.com, 2019)

3.1.4 Photocatalytic activity studies

The recovery of noble metals is quite complicated, and visible light-induced photochemical reduction of metal ions to nanoparticles (fig. 3.3) is a promising technology that does not require an addition of any other toxic or hazardous chemicals to the mixture. On the other hand, separation of nanoparticles is easier, than, for instance, desorption of the metal ions back to the solution. The photoreduction process also is quite selective, especially, if

photocatalyst has undergone specific pre-treatment or modification towards selectivity enhancement. (Grzelczak and Liz-Marzan (2014), Zhou et al., 2016)

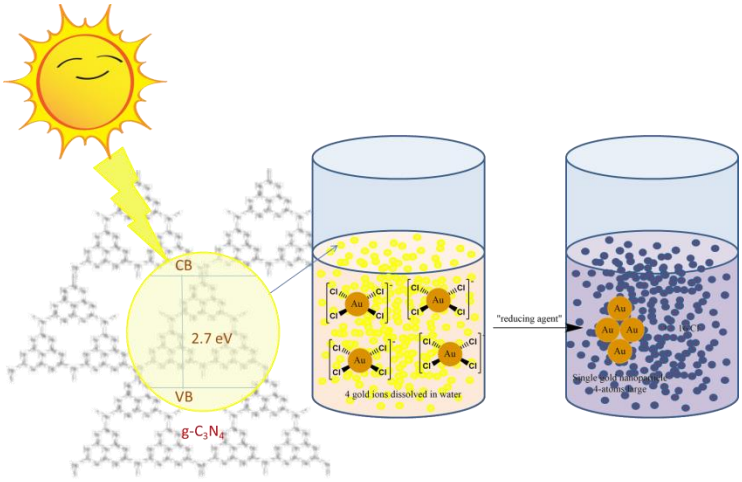

Figure 3.3. Photoreduction of $AuCl_4^-$-ions to Au nanoparticles on g-C_3N_4

Gold and platinum were considered as two representatives of the noble metal group that could be studied for the photoreduction in the presence of synthesized graphitic carbon nitride. They have been used for multiple studies as the doping agents for the photocatalysts (An et al., 2010; Chen et al., 2008; Tian and Tatsuma, 2005), although were rarely reported in regard of the recovery process development (Guo et al., 2014).

For the theoretical process modelling, all the possible reactions and their redox potentials vs. SHE (eq. 3.8 – 3.21) have been considered to understand the processes under irradiation in the presence of the catalyst. (Armstrong et al., 2013)

$$Au^{3+} + 3\bar{e} \rightarrow Au^0 \quad E = 1.52\,V \tag{3.8}$$

$$Au^{3+} + 2\bar{e} \rightarrow Au^+ \quad E = 1.36\,V \tag{3.9}$$

$$Au^+ + \bar{e} \rightarrow Au^0 \quad E = 1.83\,V \tag{3.10}$$

$$AuCl_4^- + 3\bar{e} \rightarrow Au^0 + 4Cl^- \quad E = 0.99\,V\ or\ 1.002V \tag{3.11}$$

$$PtCl_4^{2-} + 2\bar{e} \rightarrow Pt^0 + 4Cl^- \quad E = 0.73\,V \tag{3.12}$$

$$PtCl_6^{2-} + 2\bar{e} \rightarrow PtCl_4^{2-} + 2Cl^- \quad E = 0.68\,V \tag{3.13}$$

$$Cl^- \rightarrow Cl^{\cdot} + \bar{e} \quad E = -2.432\,V \tag{3.14}$$

$$OH^- + H^+ \rightarrow OH^{\cdot} + e^- + h^+ \quad E = 2.73\,V \tag{3.15}$$

$$H^+ + \bar{e} \rightarrow H^{\cdot} \quad E = -2.32V \tag{3.16}$$

$$O_2 + \bar{e} \rightarrow O_2^{\cdot -} \quad E = -0.16\,V \tag{3.17}$$

$$O_2^{\cdot -} \rightarrow H_2O_2 \quad E = 0.94\,V \tag{3.18}$$

$$O_2 + 2e^- + 2H^+ \rightarrow H_2O_2 \quad E = 0.68\,V \tag{3.19}$$

$$O_2 + 4e^- + 4H^+ \rightarrow H_2O \quad E = 1.23\,V \tag{3.20}$$

$$EtOH + h^+ \rightarrow Et^{\cdot}OH \quad E = -0.94\,V \tag{3.21}$$

Since the valence and conduction bands positions of g-C_3N_4 are known to be +1.4 eV and -1.3 eV, respectively, it is found that the Au and Pt reduction processes are thermodynamically feasible over this photocatalyst. From the summarized energy potentials scheme (fig.3.4), it is observable that the formation of superoxide radical as a result of the interaction of photoformed electron with oxygen molecule (eq.3.17) is thermodynamically favorable. This process is competitive to metal ions reduction and dissolved oxygen has to be removed from the liquid by nitrogen gas purging for sufficient time period. It also should be noted that neither interactions of hydrogen, chloride or hydroxyl-ions photoformed hole is not possible from thermodynamic point of view. Indeed, for a proper redox reaction proceeding, the hole scavenger like ethanol (EtOH), methanol (MeOH) or ethylenediamine tetraacetic acid (EDTA) is required.

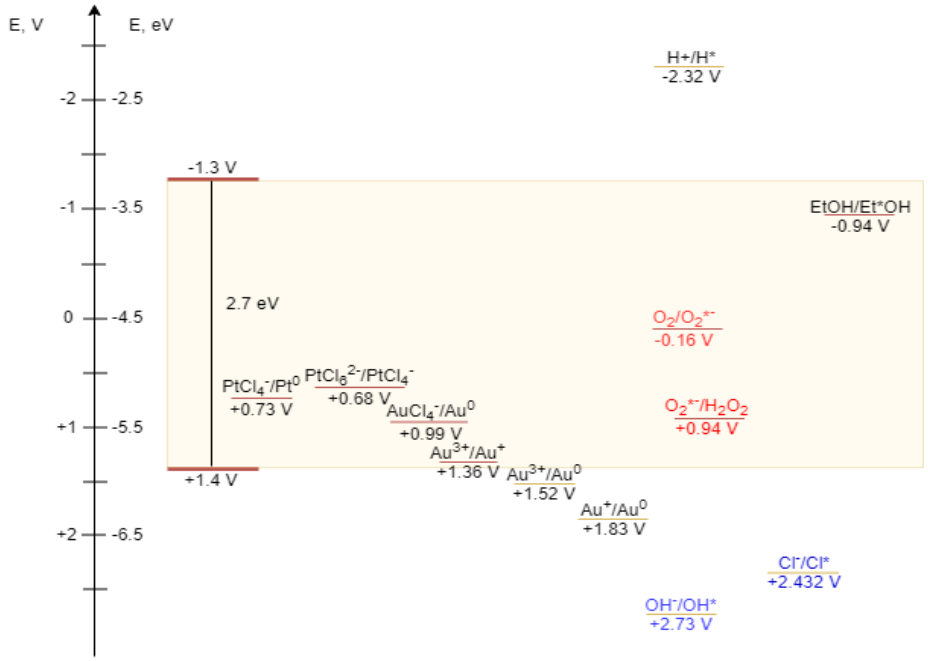

Figure 3.4. Redox potentials of possible reactions and g-C_3N_4 VB-CB energy position

Photocatalytic properties of the materials were tested towards activity in the processes of noble metal ions' reduction. The experiment consisted of two principal parts of the photocatalytic process itself and the measurement part (fig.3.5). Photocatalytic set-up included light source 300W Xe-lamp MAX-350 which irradiated with the coherent beam capped reaction vessels with liquid phase and photocatalyst in powder form. To keep the conditions in all the volume uniform during the process, magnetic stirring was applied.

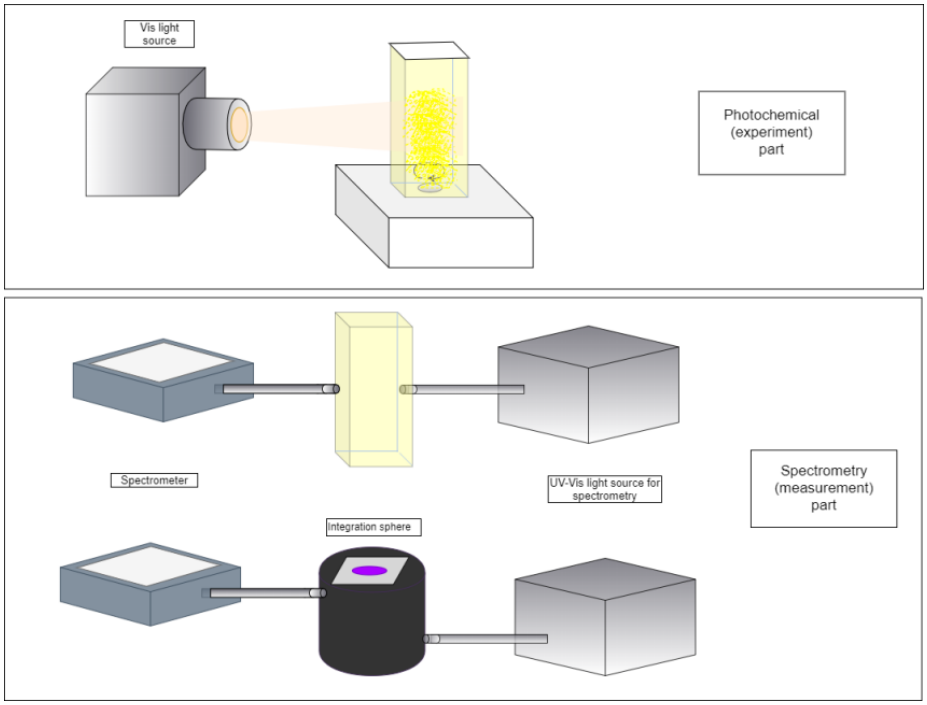

Figure 3.5. Experimental setup: reaction and measurement parts

Aqueous solution of tetrachloroauric acid and hexachloroplatinic acid at pH=0-1 (adjusted by HCl) were used in the photoreduction process. The initial concentration of the metal ions for both acids was 100 μM. The catalyst loading was 5 g L^{-1} for each sample. Ethanol aqueous solution was used in quantity of 25% (v/v) as a hole scavenger. In order to eliminate competitive oxygen reactions, the mixture was purged with the N_2 gas: in experiments with ethanol, acid and ethanol were purged for 10 min each separately and, after that, ethanol was added to the acid and the mixture was purged, additionally, for 10 min more; in experiments without ethanol, acid solution was purged for 30 min. Furthermore, to maintain inert atmosphere during all the experiment, the reaction volume was split onto volumes, required for each measurement point. Thus, after purging with N_2 gas, the solution was poured into 4 mL disposable polystyrene spectrophotometer cuvettes and covered with a cap.

For adsorption-desorption equilibrium establishment all the solutions were stirred in dark for 60 min. After that, reaction vessels were irradiated for 90 min with light intensity of 50 mW cm^{-2}. All the experiment crucial parameters mentioned above are summarized in the Table 3.1.

During the irradiation procedure, the concentration change was monitored at specific time points: initial concentration, 30 min and 60 min of adsorption, 20, 40, 60 and 90 min of irradiation. For each measurement point, one cuvette filling was centrifuged for 20 min at 6000 rpm and, after that, supernatant was checked for the remaining concentration of the metal ions, while powders were collected for the UV-VIS DRS measurement to detect any changes before and after irradiation, such as SPR appearance and its evolution. Some of the powders were also checked afterwards with HR-TEM to study nanoparticles size and shape characterization.

Table 3.1. Photoreduction setup and experiment parameters

Parameter	**Units**	**Value**
Vessel volume	mL	4
Concentration	μM	100
Catalyst loading	g L^{-1}	5
Adsorption time	min	60
Irradiation time	min	90
Distance	cm	30
Light intensity	mW cm^{-2}	50

Changes in solution concentration in time, namely the efficiency (percentage of noble metal ions reduction E, %), were calculated as the ratio between the concentration of metal ions in solution (C_i) at specific time spots i to the initial concentration of the solution (C_o) multiplied by 100 % (eq.3.22):

$$E = \frac{C_i}{C_o} \cdot 100\% \, . \tag{3.22}$$

To prove the photocatalytic nature of noble metals reduction, control experiments had to be performed:

- blank experiments (in the absence of photocatalyst) to detect the noble metals ions stability under irradiation;

- blank experiments in dark;

- dark experiments of the adsorption over the catalyst during experiment period (150 min);

- dark blank with thermostating at 30^{o}C was performed to study the thermal effect on the reaction kinetics.

3.2 Discussion of results

Synthesis of graphitic carbon nitride polymer can be performed using various procedures. The different materials and conditions for graphitic carbon nitride production were applied to investigate the influence of the synthesis procedure on their physical and chemical properties. As reported in literature review, variation of synthesis conditions affects materials C/N ratio, crystallinity and structure. In this specific study, four different samples were synthesized using melamine, DCDA, urea and MCA complex as a precursor noting that the same thermal treatment, the same polymerization time and temperature were applied for all of them. It is clear that the resulting powders from different precursors yielded g-C_3N_4 materials exhibiting the different appearance, texture (fig.3.6) and color (from light yellow to intense yellow and beige).

It is also notable that DCDA and urea samples boiled more than the melamine and MCA samples. During grinding process the higher electrostatic nature of the urea and MCA samples was noted. The yield of all four samples was as follow: melamine – 63%, DCDA – 51%, Urea – 5%, MCA – 15%.

a b c d

Figure 3.6. Samples after heating at 550 ^{o}C for 4 hours from different precursors: a) melamine, b) DCDA, c) urea and d) MCA

3.2.1 Optical and structural characteristics of the samples

As far as the present study focuses on polymeric powders, the most accurate way to study optical properties of the sample as recalculation of the absorption spectra (fig.3.7a) of powders from their diffuse reflectance spectra (fig.3.7b). The bandgap energies values of synthesized materials were obtained from the absorption spectra through calculation of the absorption coefficient. Moreover, a between the precursor and optical data of the products was established. The increase in absorbance of the materials in the range of 400 – 450 nm as well as yellow color of the powder correlate with the data reported by different authors earlier.

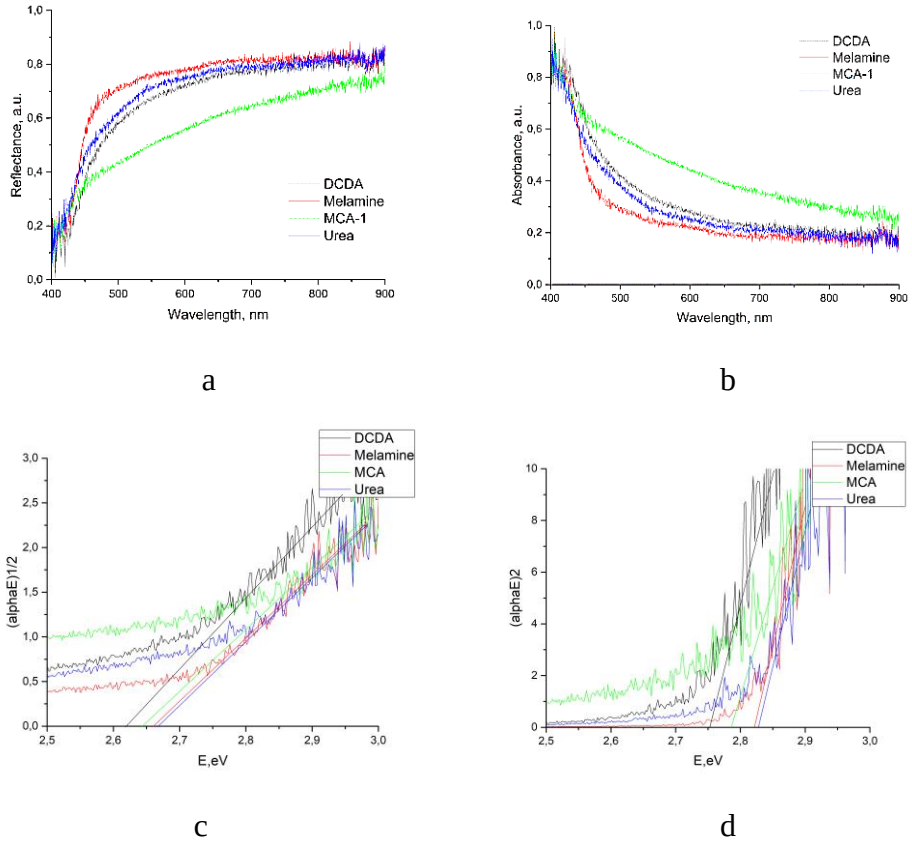

Figure 3.7. Diffuse reflectance spectra (a), recalculated absorption spectra (b), $(\alpha h\nu)^{1/2}$ vs E (c) and $(\alpha h\nu)^{2}$ vs E (d) dependencies of synthesized materials

The bandgap energy of synthesized g-C_3N_4 was calculated from the dependence of $\alpha \cdot h\nu^{1/2}$ vs E for indirect and $\alpha \cdot h\nu^{2}$ vs E for direct electron transitions. It is supposed that the transitions are mostly indirect as reported in the literature. From fig.3.7c and d, it is observable that bandgap energies slightly varied for different samples.

Calculated bandgap energies of the materials were considered as relative to the ones reported in the literature before and are summarized in Table 3.2.

Table 3.2. Calculated values of synthesized g-C_3N_4 optical properties

Transition type		DCDA	Melamine	MCA	Urea
Indirect	$(\alpha h\nu)^{\frac{1}{2}}$	2.6 eV	2.7 eV	2.6 eV	2.7 eV
Direct	$(\alpha h\nu)^{2}$	2.8 eV	2.8 eV	2.8 eV	2.8 eV

The specific surface area and pore volume using N_2 gas adsorption-desorption isotherms was obtained by BET and BJH methods (fig. 3.8), respectively. Surface area and porosity of the material are crucial parameters of the photocatalytic processes, owing to the constraints of the active sites abundance and their accessibility. The results have shown that melamine and DCDA samples possessed the lower surface area values (4.41 and 5.67 m^2 g^{-1}) and almost no pores were noted, meaning that those grains are dense non-porous particles of the polymer. The other two samples of urea and MCA showed one order of magnitude higher surface area values (41.6 and 57.8 m^2 g^{-1}, respectively) with the presence of micro- and mesopores (diameter is around 2 and 90 nm).

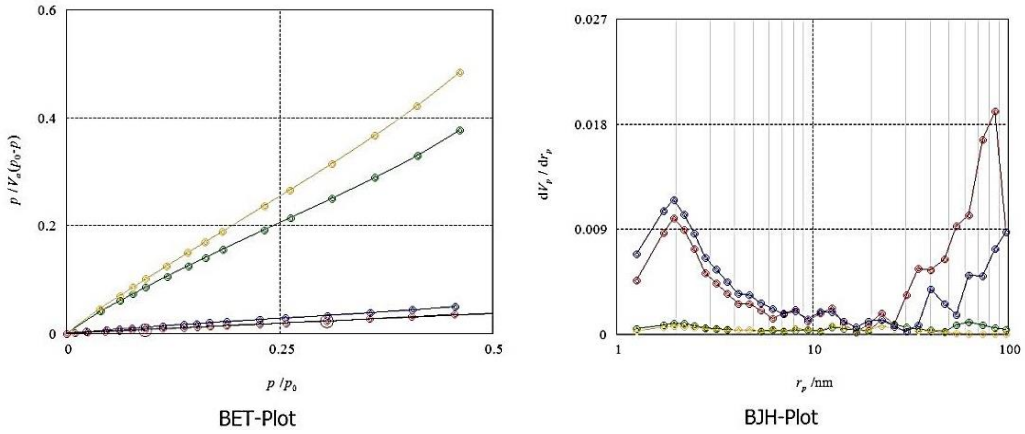

Figure 3.8. Surface area and pore size measurements

Synthesized powders have been proven to be graphitic carbon nitride by measured X-ray diffraction patterns, due to the characteristic *2θ* peaks presence: high peak at 27.4^o which corresponds to (002) plane of graphitic materials and interlayer stacking peak signed for aromatic materials and small *2θ* peak at 13.22^o that corresponds to the structural packing motif of (100) plane. It is observable from fig. 3.9 that all of the sample powders are crystalline, but not with the same crystallinity degree: melamine and DCDA samples are more

crystalline with bigger single crystal size, when urea and MCA samples show the polycrystalline nature with numerous defects presence and very small crystal size (Table 3.3). Small drifting of *2θ* peak and all the calculated values from the ones given in literature has been also observed, which may be ascribed to the difference in conditions of the synthesis procedure. Conclusively, in terms of semiconductive properties, the samples obtained from melamine and DCDA could be considered as the promising sample.

Table 3.3. Crystallinity parameters for all the synthesized samples

Sample	27.40^{o}			13.22^{o}	
	peak shift	d-spacing, Å	crystal size, nm	peak shift	d-spacing, Å
DCDA	27.20	3.28	5.28	12.90	6.86
Melamine	27.15	2.28	5.84	13.30	6.66
MCA	26.45	3.34	2.02	12.95	6.84
Urea	26.50	3.36	2.24	13.10	6.76

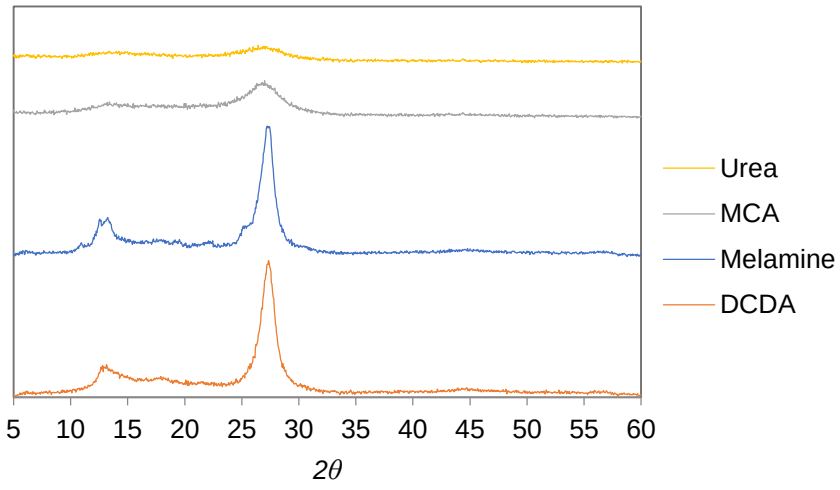

Figure 3.9. X-Ray diffraction patterns of polymers as synthesized

The suggested structure of particles was partly proved by the scanning electron microscopy images (fig. 3.10). Melamine sample (fig. 3.10a) has yielded in layers of dense crystalline particles, when DCDA (fig. 3.10b) looks like boiling polymer structure with blocked pores structure. Urea sample (fig. 3.10c) yielded in spongy structure with really small size of particles and MCA (fig. 3.10d) has resulted in structurally organized particles of spherical shape.

It is noticable that during thermal treatment all synthesized materials obtained the developed structure that is built from relatively small particles. However, in case of urea and MCA samples, structure is more uniform, than for DCDA and melamine samples.

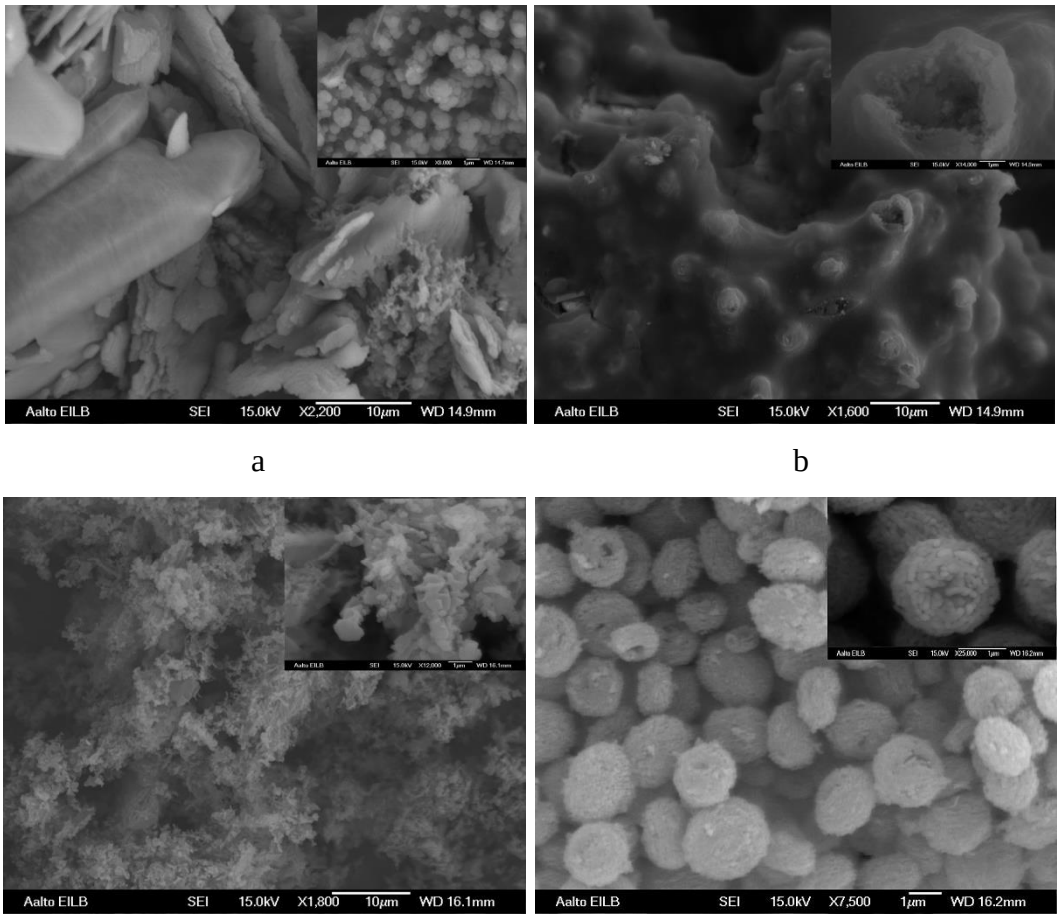

a b

c d

Figure 3.10. SEM images of (a) melamine, (b) DCDA, (c) urea and (d) MCA samples

HR-TEM was used for imaging of the samples that have undergone the photoreduction of Au ions to nanoparticles experiment (fig. 3.11). As it was expected from previous characterization results (mentioned above), the sample obtained from melamine has been represented by various structure and shape of the material grains (fig. 3.11a, b, c), but mostly those were non-porous and consisted of tightly packed layers of heptazine. The photocatalytically formed Au nanoparticles coverage was non-uniform among the particles and mainly nanoparticles were observed on the surface of the catalyst's particle. In case of DCDA sample (fig.3.11d, e, f), the polymeric porous structure was observed. It was covered with more Au-nanoparticles that were more uniformely distributed and particles also could reach the inner pores structure of the material. For sample obtained from urea (fig.3.11g, h, i),

the least amount of Au-nanoparticles was observed and structure of the material itself was recognizable as big layered flakes of the polymer compared to the other samples. MCA sample was not tested by TEM imaging, due to its comparatively low photocatalytic activity.

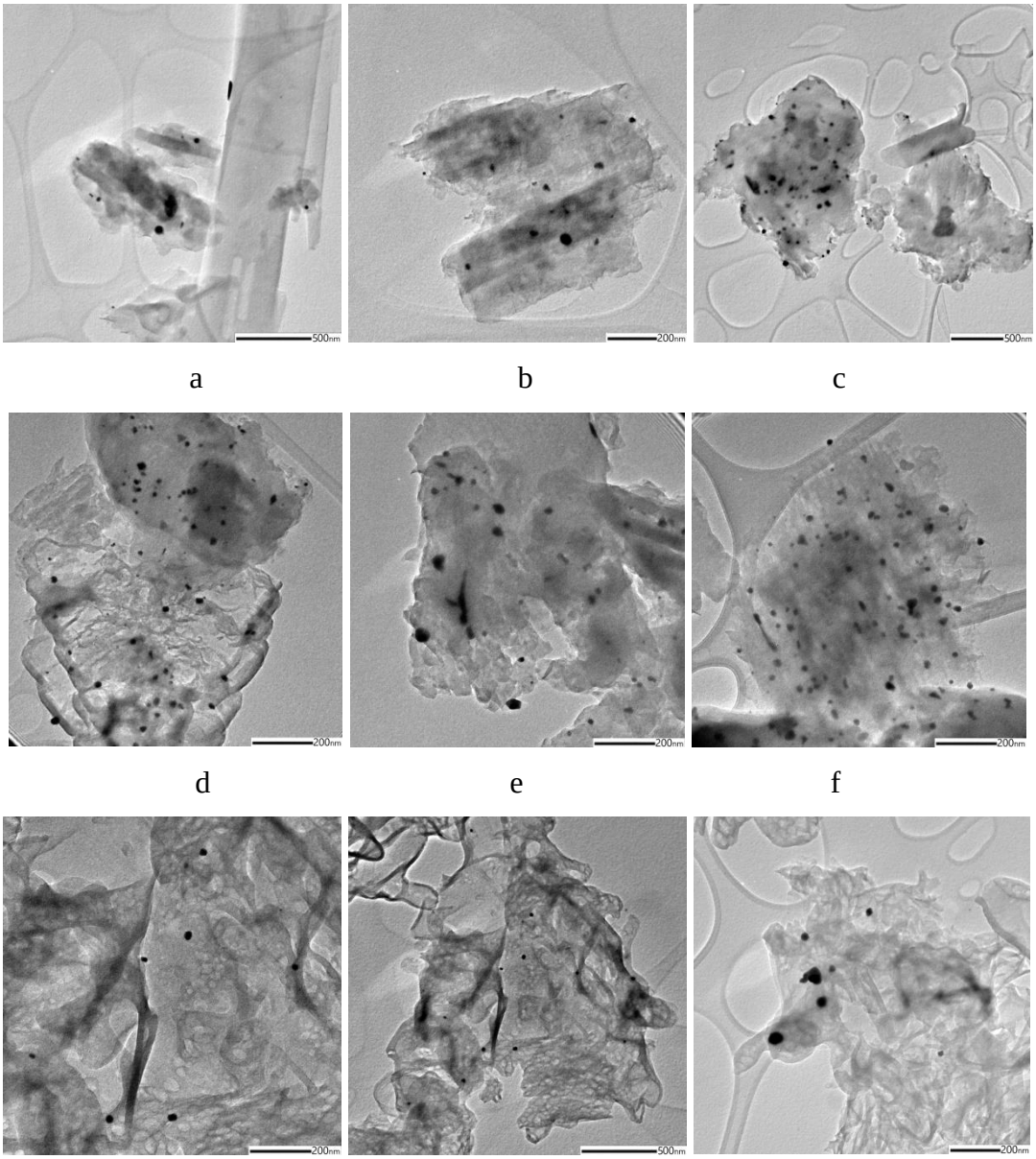

Figure 3.11. HR-TEM images of samples after Au photoreduction obtained from: melamine (a, b, c), DCDA (d, e, f) and urea (g, h, i)

The energy-dispersive X-ray spectroscopy (EDS) detector from HR-TEM was used for elemental mapping and C/N ratio was roughly recalculated from the data from EDS. The EDS spectra of different powders are presented on fig.3.12 and recalculated C/N ratios are summarized in Table 3.4.

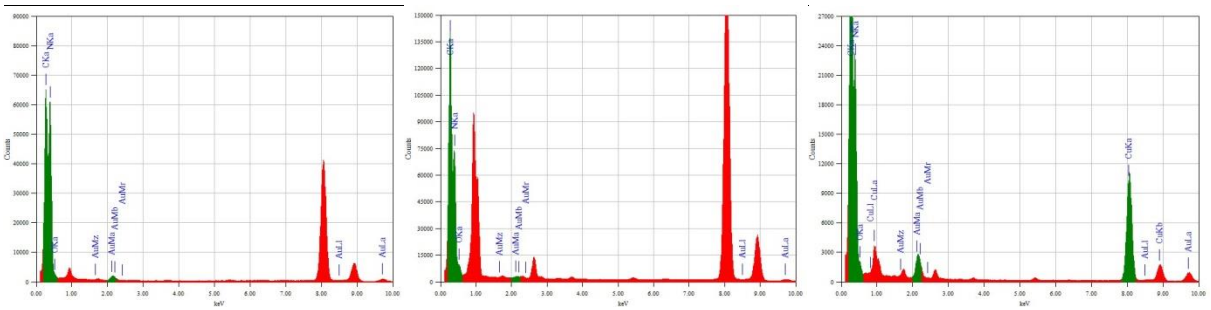

a b c

Figure 3.12. Melamine (a), DCDA (b) and urea (c) EDS spectra

Table 3.4. C/N ratio estimation from EDS mapping

Peak intensity	C	N	C/N
Melamine	65000	61000	1.06
DCDA	147000	74000	1.99
Urea	48000	23000	2.08

The ratio of C/N increased from 1.06, 1.99 to 2.08 in the range from melamine, DCDA to urea. When melamine was used, the ratio reached the values reported in the literature (0.7 – 1.0 (Wang et al., 2015)). The sharp decrease in the nitrogen content can be caused by the presence of the compressed air during thermal treatment leading to the substitution of nitrogen by oxygen. An additional reason for enhanced nitrogen release from the structure could be the chemical structure of small molecules of DCDA and urea compared to melamine.

SEM and TEM-EDS results do correlate with the crystallinity, surface area and porosity data, obtained from XRD and N_2 adsorption/desorption isotherms. In turn, the most promising for photocatalytic activity perspective could be suggested to be DCDA and melamine samples.

3.2.2 Photocatalytic activity of obtained samples

Photocatalytic activity of the materials was tested on photoreduction of Au and Pt ions from tetrachloroauric and hexachloroplatinic acids, respectively, under visible light irradiation (420 – 600 nm). Each material was tested with two metal solutions (except MCA sample due to its low resulting powder yield) in the dark and under irradiation. Additionally, dark and light blank measurements without the catalyst were conducted. Moreover, thermal effect and

influence of the hole scavenger presence were established (fig.3.12) where the effect of the presence of 25% (v/v) EtOH and irradiation is pronounced, with removal of near 80% of metal ions for both Au and Pt while the temperature increase up to 30 ^{o}C had less effect.

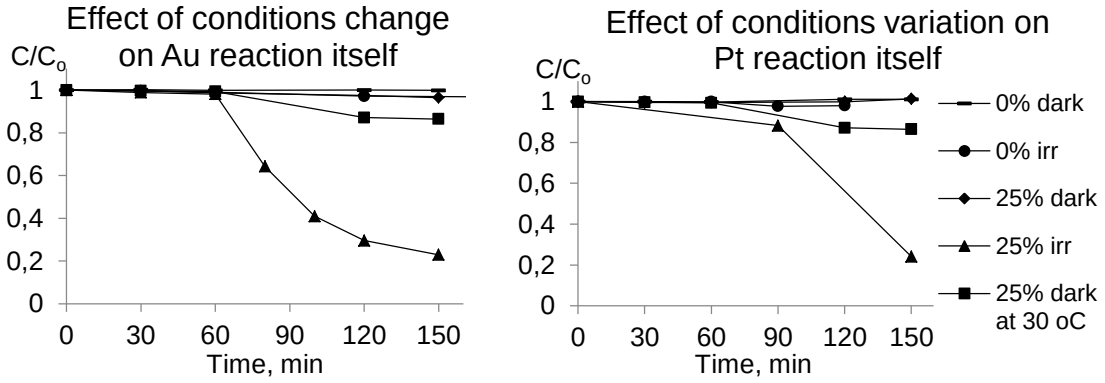

Figure 3.13. Influence of different experimental conditions on the concentration change of gold and platinum ions in liquid phase during blank (without the catalyst) experiment

In experiments without the hole scavenger, the metal ions were removed from the liquid phase with efficiency up to 96.6% for Au and 43% for Pt (Table 3.5 and 3.6) without visible solution color change meaning that no nanoparticles were formed. EDS results clearly show that no formation of Au-nanoparticles took place, but uniform adsorption of gold ions occurred (fig. 3.14). The highest adsorption of the Au ions was observed on the surface of the urea and MCA-based samples that can be explained by the higher SSA of these materials.

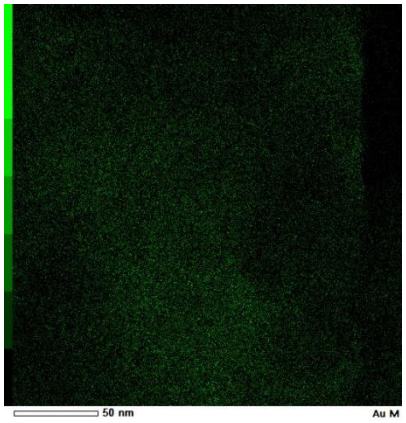

Figure 3.14. EDS mapping of the Au abundance on the DCDA sample after the irradiation for 2 hours without the ethanol addition

The experiments under irradiation yielded higher removal rate of the targeted metal ions than the experiments in dark. Moreover, the suggestion about the photocatalytic reduction of Au^{3+} ions to Au^{+} by photoformed electrons can also be done, taking into account

that the redox potential of this reaction under irradiation in the presence of the catalysts is thermodynamically suitable. (eq.3.23 – 3.24) (Linnik et al., 2013). The photoformed electron could interact with Au^{3+} with the formation of Au^{2+} (eq. 3.23) that could be disproportionated to Au^{+} and Au^{3+} (eq. 3.24). As a result, the next photoformed electrons have to reduce again Au^{3+} ions. That is why the final reduction step of Au^{+} to Au^{0} is not occurring. Concurrently with the reduction process, the photoformed hole can interact with water molecules (as a hole scavenger) leading to O_2 production (thermodynamically possible) (eq. 3.25). This oxygen evolution reaction could limit the Au-ions reduction, due to the competitive electron interaction with O_2 yielding superoxide radicals (eq. 3.17). It can be the second reason why Au^{0} formation was not observed when water acted as a hole scavenger.

$$(HAu^{3+}Cl_4) + 1\bar{e} \rightarrow (HAu^{2+}Cl_3 \dots Cl) \quad (3.23)$$

$$(HAu^{2+}Cl_3) \rightarrow HAu^{3+}Cl_4 + HAu^{+}Cl_2 \quad (3.24)$$

$$H_2O + 4h^{+} \rightarrow O_2 + 4H^{+} \quad E = 0.81\ eV \quad (3.25)$$

Table 3.5. Efficiencies of the Au^{3+} ions removal from the liquid phase in photoreduction experiments (in experiments given in bold color change has been observed)

Au	**Under light**		**In dark**	
EtOH %-v	0%	25%	0%	25%
Removal efficiency, %				
Melamine	52.0	**79.4**	22.2	6.9
DCDA	57.3	**94.2**	25.5	11.7
MCA	94.6	**93.9**	-	**13.6**
Urea	96.6	**90.2**	47.2	**14.3**
Blank	3.2	77.1	0	3.5

In the case of the hole scavenger presence, namely 25% (v/v) EtOH in the reaction mixture, the concentrations of both metals were more intensively decreased under irradiation. In experiments with Au, the color change of liquid phase was observed as a proof of the Au-nanoparticles formation (fig.3.15).

Table 3.6. Efficiencies of the Pt^{4+} ions removal from the liquid phase in photoreduction experiments photoreduction experiments

Pt	**Under light**		**In dark**	
EtOH %-v	0%	25%	0%	25%
Removal efficiency, %				
Melamine	17.0	44.5	0	0
DCDA	18.5	83.5	4.0	7.7
Urea	43.0	90.5	9.0	3.6
Blank	3.2	75.8	0	0

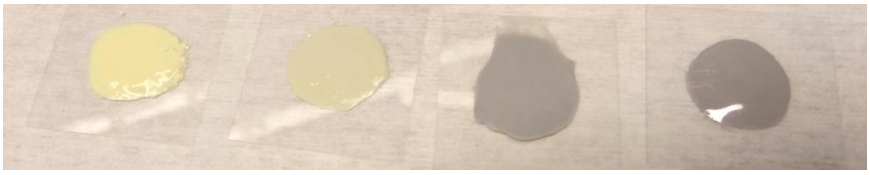

60 min ads 20 min irr 40 min irr 60 min irr

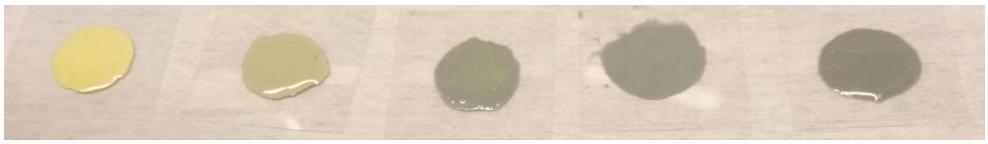

60 min ads 20 min irr 40 min irr 60 min irr 90 min irr

Figure 3.15. G-C_3N_4 powders after centrifugation at specific time points of the measurement of Au photoreduction on melamine sample (top image) and DCDA (bottom)

Contrary to the irradiation procedure without ethanol, the reduction of Au^{3+} ions in the presence of EtOH proceeds to Au^0 and ethanol plays the key role in it. It could be suggested, that ethanol molecules after interaction with photoformed hole undergoes to hydroxyethyl radicals ($CH_3CH^{\cdot}OH$). This radical is unstable and transforms to acetaldehyde with additional electron injection to the conduction band of the catalyst. The reduction of Au^{3+} goes faster, owing to the appearance of two electrons in the conduction band. The presence of additional electrons from hydroxyethyl radicals can lead to complete reduction of Au-ions to Au-nanoparticles. (Rusina et al., 2005)

$$h_r^+ + CH_3CH_2OH \rightarrow CH_3CH^{\cdot}OH + H^+ \quad E = -0.94 \tag{3.26}$$

$$CH_3CH^{\cdot}OH \rightarrow CH_3CHO + e_r^- + H^+ \tag{3.26}$$

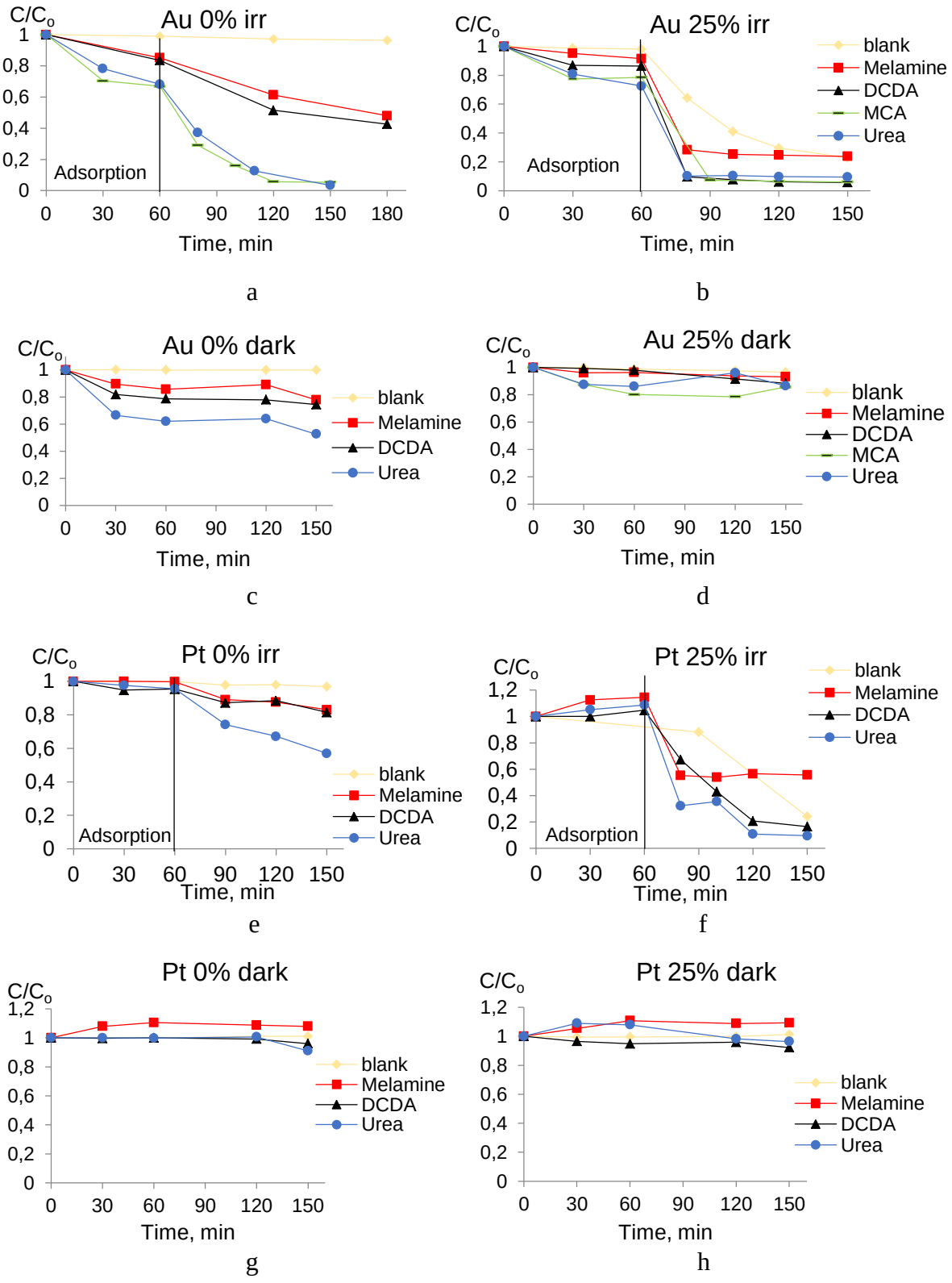

Figure 3.16. Photoreduction kinetics for Au (a, b, c, d) and Pt (e, f, g, h) ions removal from liquid phase in presence or absence of alcohol and light

Kinetics of all the experiments have been plotted (fig.3.16). The blank experiments presented in fig. 3.16 show lower removal efficiency without light and hole scavenger.

From the kinetics curves (fig. 3.16 a, b), it can be seen that the powders obtained from urea exhibited the highest ions removal activity with and without EtOH taking into account that almost no Au ions were detected after 60 and 20-25 min of irradiation without EtOH and with EtOH, respectively. It can be noted that 90% of Au-ions were removed after 60 min of irradiation in the presence of EtOH while only 40% of Au-ions disappeared after longer irradiation time (90 min) without EtOH. It points on the increased rate of the reaction in the presence of 25% EtOH. The observed color change happened mostly between 20 and 40 min of irradiation and, according to the kinetics plotting (fig.3.16b), reaction almost stopped after 60 min under light.

Despite the intensified decrease of tetrachloroauric acid peak on UV-vis spectra liquid phase (fig. 3.17), no surface plasmon resonance (SPR) was observed there, meaning that g-C_3N_4 powders were acting as the nucleation cites for the Au-nanoparticles formation and the process of Au photoreduction was interfacial.

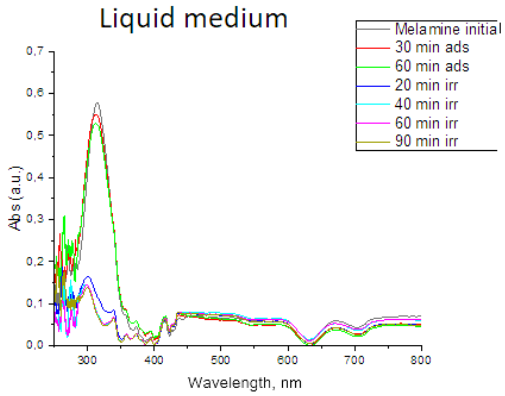

Figure 3.17. UV-VIS spectra of the liquid phase at different experiment points from the Au photoreduction on melamine-based powder experiment with 25% (v/v) EtOH

DRS spectra of the powders were measured after the centrifugation of the reaction solution, in order to evaluate the performance of different samples for the targeted process. Moreover, to present SPR development in more suitable form, the initial spectrum was subtracted from the time specific measurement point's spectra and those results were plotted against wavelength value (fig.3.18).

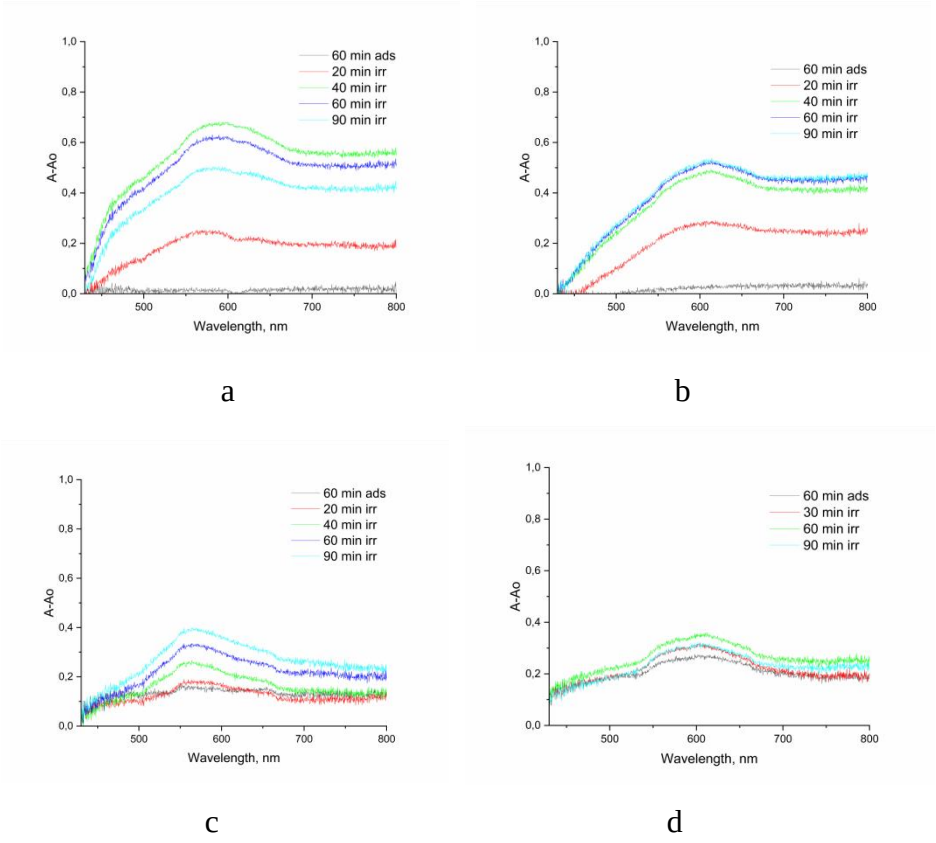

Figure 3.18. SPR development on powders during the photoreduction experiment on melamine (a), DCDA (b), urea (c) and MCA (d) samples (recalculated from VIS-DRS of the powders)

The most extensive surface plasmon resonance growth was observed in case of experiments with melamine, DCDA and urea based g-C_3N_4. For melamine sample, SPR showed the band from 550 to 660 nm and, consequently, particles of different size and shape could be formed there. Violet subtone of the powders after the centrifugation also indicates the medium size of the particles in range of 60 – 100 nm. For DCDA sample, the SPR growth was more stable and it showed the broad band at 550 – 650 nm and blue subtone of the sample powder after the experiment. The suggested size could be about 100 nm and more even with agglomerates formation.

In case of urea sample, the formed nanoparticles were more uniform in size around 60 nm, although the SPR evolution was lower. Also, the color change of the powders was less drastic and developed slower till the end of the experiment. Thus, despite the higher Au-ions removal rate from the liquid phase, the conclusion about lower conversion of Au ions into Au-nanoparticles could be done. For MCA sample, the surface plasmon resonance developed

the worst, if compared to the other samples. It still had the band of 550 – 650 nm, however, the efficiency of the Au-nanoparticles formation was the lowest.

Presence of Au-nanoparticles was proven by the HR-TEM (fig.3.11) and EDS mapping (fig. 3.18). From TEM images (fig. 3.19) the variety in Au-nanoparticles shape and size is observable. All together nanospheres, nanorods, nanocubes and clusters were observed.

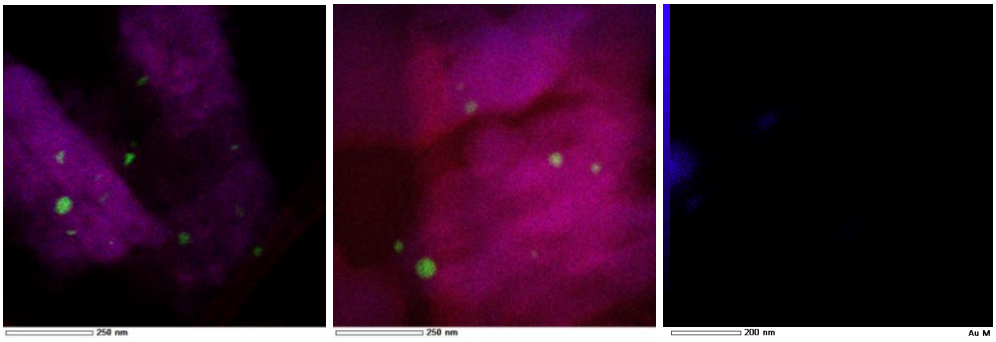

a b c

Figure 3.18. EDS mapping of C, N and Au elements on melamine (a), DCDA (b) and urea (c) sample after photoreduction in the presence of 25%-v EtOH

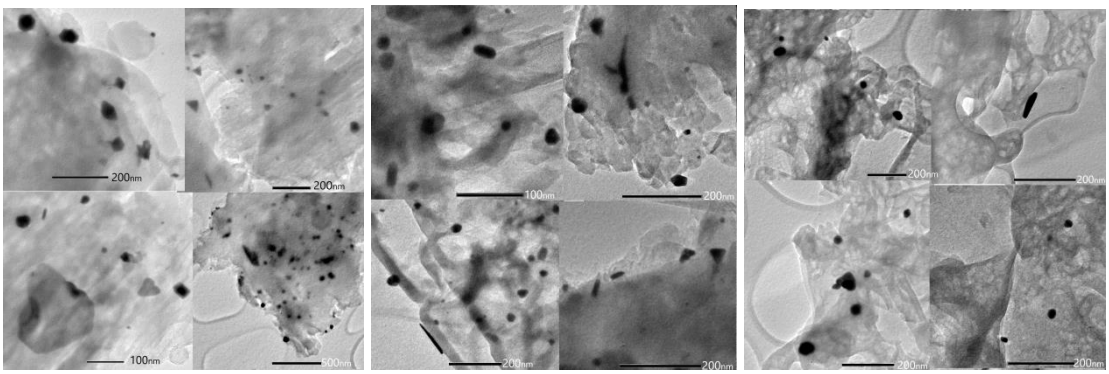

a b c

Figure 3.19. TEM images of Au nanoparticles formed on melamine (a), DCDA (b) and urea (c) sample after photoreduction in the presence of 25%-v EtOH

Additionally, DRS spectra of the urea with/without EtOH and under irradiation/in dark were measured to study the conditions influence on the Au-nanoparticles surface plasmon resonance development (fig.3.20). It was clearly seen that nanoparticles were formed only in the case of synergic effect of the light and ethanol presence and none of them could be enough by themselves to form nanoparticles.

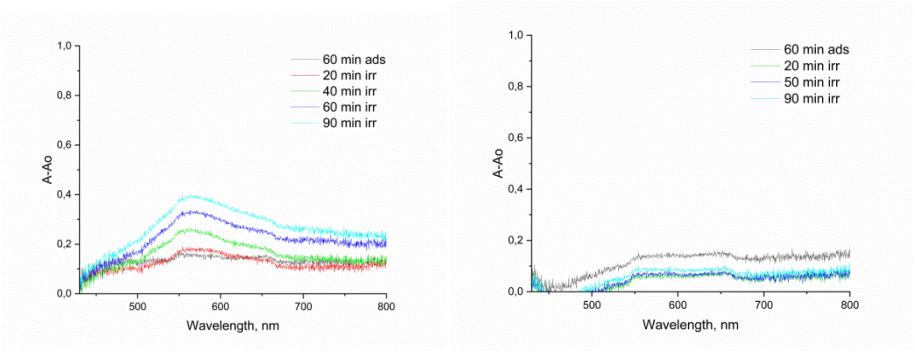

a b

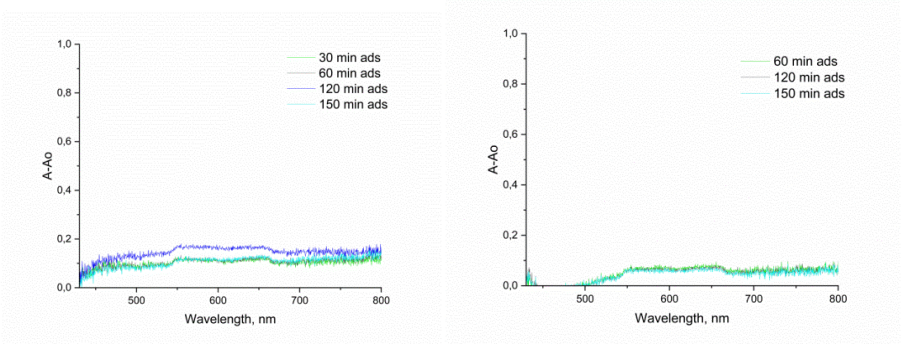

c d

Figure 3.20. Comparison of different conditions influence on SPR evolution on urea sample: under irradiation with 25%EtOH (a) and without (b), in dark with 25%EtOH (c) and without (d)

It is also notable that Au nanoparticles could have been easily separated from the reaction solution by centrifugation and the fraction with higher content of the nanoparticles was concentrated between the heavy solid phase and below the liquid phase (fig. 3.21).

Figure 3.21. Centrifuged photocatalyst powder, nanoparticles and liquid phase after Au photoreduction

In the other part of the study related to the Pt ions reduction to nanoparticles, no nanoparticles formation was observed. Despite quite high adsorption rates, neither change of

color nor SPR evolution was observed. Presence of ethanol under irradiation caused intensification of Pt-ions concentration decrease, however, without any transformation expected from the theoretical process evaluation. On the other hand, the photoreduction of Au-ions to nanoparticles has proven to be selective what, undoubtedly, is an advantage in the perspective of selective gold recovery.

4 CONCLUSIONS

In this thesis, the different precursors were used as the source for tri-*s*-triazine layers synthesis to investigate the influence of the nature of different precursors (Melamine, DCDA, Urea, MCA) on the structure, morphology, composition and photocatalytic properties of g-C_3N_4. Depending on the precursor, different textural features were observed: non-porous grains for melamine based sample, particles with the blocked pores for DCDA, sponge built from the big layered flakes for urea and organized spherical structure for MCA. Apparent crystallinity of the synthesized materials increased in the order of the precursors melamine>DCDA>MCA>Urea, while the specific surface area decreased with increasing crystallinity. The different C/N ratio for the melamine, DCDA and urea-based samples can be explained by the varied synthesis conditions: the more sophisticated nature of the precursor led to the higher nitrogen content in the final product.

The efficiency of photocatalytic reduction of Au^{3+} ions to Au^0 nanoparticles was successful under irradiation in the presence of 25% (v/v) EtOH as hole scavenger as confirmed by the color change of mixture during the experiment and TEM images afterwards. From the DRS measurements that are supported by TEM images, the formation of different shapes and sizes of nanoparticles depending on the sample were detected for ethanol-containing systems. No SPR was observed in the liquid phase by UV-VIS spectroscopy indicating the interfacial nature of the reaction.

In the absence of ethanol but under light, efficient removal of Au-ions can be explained by both the adsorption (confirmed by dark experiments) and photocatalytic reduction of Au^{3+} ions to Au^+ ions (supported by EDS mapping). Moreover, the formation of Au nanoparticles in this case was hard to be achieved due to the appearance of O_2 from the oxidative pathway (photooxidation of water molecule to oxygen one).

In general, it seems that the reaction pathways for ethanol-containing and EtOH-free systems followed the different route. The study showed that the presence of ethanol was one of the main points for Au-nanoparticles formation. The efficiency of Au^0 production was different and estimated as DCDA>melamine>urea>MCA that can be explained by better crystallinity of DCDA and melamine compared to the other samples.

For Pt^{4+} ions photoreduction, no nanoparticles formation was observed in the experiments with or without ethanol, under irradiation or in the dark as opposed to theoretical

process thermodynamics evaluation. However, the high removal efficiency of Pt^{4+} ions was noted under irradiation in the presence of 25% (v/v) EtOH suggesting the intensified adsorption of Pt-ions on the materials' surfaces or the parallel formation of Pt intermediate oxidation states.

For the future investigation numerous aspects and parameters can be considered. Manipulation on the synthesis conditions by the change of the atmosphere from air to nitrogen or argon, change of thermal treatment temperature, polycondensation time or precursors could positively affect the properties of the photocatalyst and increase the process efficiency. Variation of the EtOH quantity in the mixture for photocatalysis may lead to the process OpEx decrease in terms of industrial application (when less quantity of ethanol used) or better process performance (when higher content of ethanol used). Also, other hole scavengers may be tested, in order to combine the recovery of noble metals with environmental photocatalysis as far as modern pollutants like dyes, pharmaceuticals and personal care products would simultaneously act as the electron donors for photoformed holes resulting in their degradation.

5 SUMMARY

This study was dedicated to the investigation of visible light-driven photoreduction of noble metals ions to nanoparticles, due to the high interest of industry in noble metals and REE recovery from the WEEE. Considered photocatalytic material had to be non-toxic, inexpensive, robust, visible light active and industrially applicable, at the same time.

Graphitic carbon nitride was considered as the photocatalyst for this study, due to its extensive investigation in last decade and high efficiency in water splitting, organics transformation and degradation processes. Four different precursors were used for the synthesis of the g-C_3N_4 and physical and chemical properties of the polycondesated powders were studied with different characterization techniques (XRD, SEM, HR-TEM-EDS, BET and BJH methods, VIS-DRS).

Photocatalytic reduction experiments were performed on Au and Pt ions in tetrachloroauric and hexachloroplatinic acids aqueous solutions under visible light irradiation in the inert atmosphere. Water and ethanol were used as hole scavengers. The blank and dark measurements were performed to prove the photocatalytic nature of the process.

Higher ions removal from the liquid phase was observed on the urea and MCA samples owing to their higher SSA. On the other hand, the intensity of nanoparticles formation was considered as superior for this study, so the performance of the materials would be estimated as DCDA>melamine>urea>MCA.

However, there are still different parameters of the process to be studied in future, in order to improve the process efficiency and to make noble metals photoreduction more promising for industrial implementation. Thus, the novelty of the current study should be considered as the starting point for the future investigations.

6 REFERENCES

An, C. H., Peng, S. N. and Sun, Y. G. 2010. Facile synthesis of sunlight-driven AgCl:Ag plasmonic nanophotocatalyst. *Adv Mater*, 22: 2570–2574.

Anpo, M. and Thomas, J. M. 2006. Single-site photocatalytic solids for the decomposition of undesirable molecules. *Chem. Commun*., 3273–3278, DOI: 10.1039/b606738g

Arbogast, JW, Darmanyan, AP, Foote, CS, Diederich, FN, Whetten, RL, Rubin, Y, Alvarez, MM, Anz, SJ. 1991. Photophysical properties of sixty atom carbon molecule (C60) *J Phys Chem* 95(1):11–12.

Ariga, K., Mori, T., Nakanishi, T., Hishita, S., Goldbeg, D. And Bando, Y., 2005. Preparation and Characterization of Well-Ordered Hexagonal Mesoporous Carbon Nitride. *Adv Mat*, 17, pp. 1648.

Badhwar, N., Gupta, N., Pal, B. 2013. Photochemical fabrication of transition metal nanoparticles using CdS template and their co-catalysis effects for TiO_2 photocatalysis. *Int J of Nanosc*, 12, (3): 1350020.

Bao, N. Z., Shen, L. M., Takata, T. and Domen, K. 2008. Mesoporous carbon nitride with in situ sulfur doping for enhanced photocatalytic hydrogen evolution from water under visible light. *Chem Mater*, 20: 110–117.

Bickley, R. I., Munuera, G.and Stone, F. S. 1973. Photoadsorption and photocatalysis at rutile surfaces: II. Photocatalytic oxidation of isopropanol. *J Catal*, 31: 398–407.

Butler, E. C. and Davis, A. P. 1993. Photocatalytic oxidation in aqueous titanium dioxide suspensions: the influence of dissolved transition metals. *J Photochem Photobiol A*, 70: 273–283.

Cao, S. W., Low, J. X., Yu, J. G. and Jaroniec, M. 2015. Polymeric Photocatalysts Based on Graphitic Carbon Nitride. *Adv. Mater*., 27: 2150–2176.

Carey, H., Lawrence, J. and Tosine, H. M. 1976. Photodechlorination of PCB's in the presence of titanium dioxide in aqueous suspensions. *Bull Environ Contam Toxicol*, 16: 697–701.

Chen, X., Jun, Y., Takanabe, K., Maeda, K., Domen, K., Fu, X., Antonietti, M. And Wang, X., 2009. Ordered Mesoporous SBA-15 Type Graphitic Carbon Nitride: A

Semiconductor Host Structure for Photocatalytic Hydrogen Evolution with Visible Light. *Chem of Mat*, 21(18): 4093-4095.

Chen, X., Zhu, H. Y., Zhao, J. C., Zheng, Z. T. and Gao, X. P. 2008. Visible-light-driven oxidation of organic contaminants in air with gold nanoparticle catalysts on oxide supports. *Angew Chem Int Ed*, 47: 5353–5356.

Choi, SK, Kim, S, Lim, SK, Park, HK. 2010. Photocatalytic comparison of TiO2 nanoparticles and electrospun TiO2 nanofibers: effects of mesoporosity and interparticle charge transfer. *J PhysChem C* 114(39):16475–16480.

Cui, Y., Ding, Z., Fu, X. And Wang, X., 2012. Construction of Conjugated Carbon Nitride Nanoarchitectures in Solution at Low Temperatures for Photoredox Catalysis. *Angew Chem (Int ed. in Eng)*, 51(47): 11814-11818.

Dai, K, Peng, T, Ke, D, Wei, B. 2009. Photocatalytic hydrogen generation using a nanocomposite of multi-walled carbon nanotubes and TiO2 nanoparticles under visible light irradiation. *Nanotechnol* 20 (12): 125603.

Di, J, Xia, J, Ge, Y, Li, H, Ji, H, Xu, H, Zhang, Q, Li, H, Li, M. 2015a. Novel visible-light-drivenCQDs/Bi2WO6hybrid materials with enhanced photocatalytic activity toward organicpollutants degradation and mechanism insight. *Appl Catal B* 168–169: 51–61.

Di, J, Xia, J, Ji, M, Wang, B, Yin, S, Zhang, Q, Chen, Z, Li, H. 2015b. Carbon quantum dots modifiedbiocl ultrathin nanosheets with enhanced molecular oxygen activation ability for broadspectrum photocatalytic properties and mechanism insight. *ACS Appl Mater Interfaces* 7(36):20111–20123.

Directive, E. C., 2012. Directive 2012/19/EU of the European Parliament and of the Council of 4 July 2012 on waste electrical and electronic equipment, WEEE. *Official J of the EU L*, *197*, 38-71.

Dong, Y., Liu, Y., Lu, D., Zheng, F., Fang, P., Zhang, H. 2017. Unpredictable adsorption and visible light induced decolorization ofnano rutile for the treatment of crystal violet. *Solid State Sciences*, 66: 1-6.

Dong, X. P. and Cheng, F. X. 2015. Recent development in exfoliated two-dimensional g-C3N4 nanosheets for photocatalytic applications. *J. Mater. Chem. A*, 3: 23642–23652.

Dong, F, Wang, Z, Sun, Y, Ho, WK, Zhang, H. 2013. Engineering the nanoarchitecture and texture of polymeric carbon nitride semiconductor for enhanced visible light photocatalytic activity.*J Colloid Interface Sci*, 401: 70–79.

Du, Y, Cheng, Z, Yu, Z, Do, SX, Wang, X, Liu, L. 2012. Hydrothermal synthesized bismuth ferritesparticles: thermodynamic, structural, and magnetic properties. *J Nanosci Nanotechnol*, 12(2): 1684–1687.

European Commission, 2019. *Waste Electrical & Electronic Equipment (WEEE)*, [Accessed 11 April 2019]. Available at: http://ec.europa.eu/environment/waste/weee/index_en.htm

Fan, C, Chen, C, Wang, J, Fu, X, Ren, Z, Qian, G, Wang, Z. 2015. Black hydroxylated titaniumdioxide prepared via ultrasonication with enhanced photocatalytic activity. *Sci Rep* 4:11712

Fang, J., Fan, H., Li, M. And Long, C., 2015. PER View Article Onli. *J of Mat Chem A*, 3(26): 13819-13826.

Fechler, N., Fellinger, T. And Antonietti, M., 2013. "Salt Templating": A Simple and Sustainable Pathway toward Highly Porous Functional Carbons from Ionic Liquids. *Advanced Materials*, 25(1): 75-79.

Fujishima, A. and Honda, K. 1972. Electrochemical photolysis of water at a semiconductor electrode. *Nature*, 238 (5358), 37-38.

Fujishima, A., Rao, T.N., Tryk, D.A. 2000. Titanium dioxide photocatalysis. *J Photochem Photobiol C*, 1 (1):1 – 21.

Fujiwara, H., Hosokawa, H., Murakoshi, K., Wada, Y. and Yanagida, S. 1998. Surface Characteristics of ZnS Nanocrystallites Relating to Their Photocatalysis for CO2 Reduction *Langmuir*, 14: 5154–5159.

Fulvio, P.F., Hillesheim, P.C., Oyola, Y., Mahurin, S.M., Veith, G.M. And Dai, S., 2011. ChemComm: A new era. *Chem comm (Cambridge, England)*, 48(1): 19-22.

Gao, X., Liu, E., Yang, Y., Hou, W., Kang, L., Fan, J. And Hu, X., 2013. Synthesis and charecterization of graphitic carbon nitride sub-microspheres using microwave method under mild condition. *Diamond and Related Materials*, 38: 109-117.

Ghosh, S. (ed). 2018. *Visible-Light-Active Photocatalysis: Nanostructured Catalyst Design, Mechanisms, and Applications, 1st ed.* Chapter 3: Fundamentals of Photocatalytic Water Splitting (Hydrogen and Oxygen Evolution). John Wiley & Sons. Retrieved from: https://app.knovel.com/hotlink/toc/id:kpVLAPNCD3/visible-light-active/visible-light-active.

Grzelczak, M. and Liz-Marzan, L.M. 2014. The relevance of light in the formation of colloidal metal nanoparticles. *Chem Soc Rev*, 43: 2089.

Hagen, J. 2006. *Industrial catalysis: a practical approach*/Jens Hagen, 2nd ed. Wiley: Weinheim.

Hamity, M., Lema, R. H., Suchetti, C. A. and Gsponer, H. E. 2008. UV–vis photodegradation of dyes in the presence of colloidal Q-CdS. *J Photochem Photobiol A*, 200: 445–450.

Han, Q., Wang, B., Gao, J., Cheng, Z., Zhao, Y., Zhang, Z. And Qu, L., 2016. Atomically Thin Mesoporous Nanomesh of Graphitic C3N4 for High-Efficiency Photocatalytic Hydrogen Evolution. *ACS Nano*, 10: 2745-2751.

He, F., Chen, G., Yu, Y., Zhou, Y., Zheng, Y. And Hao, S., 2015. The sulfur-bubble template-mediated synthesis of uniform porous g-C3N4 with superior photocatalytic performance. *Chemical communications (Cambridge, England)*, 51(1): 425-427.

Hong, J, Zhang, W, Wang, Y, Zhou, T, Xu, R. 2014. Photocatalytic reduction of carbon dioxide overself-assembled carbon nitride and layered double hydroxide: the role of carbon dioxideenrichment. *Chem Cat Chem* 6(8):2315–2321.

Hu, J. S., Ren, L. L., Guo, Y. G., Liang, H. P., Cao, A. M., Wan, L. J. and Bai, C. L. 2005. Mass production and high photocatalytic activity of ZnS nanoporous nanoparticles. *Angew. Chem., Int. Ed*., 44: 1269–1273.

Ihnatiuk, D. V., Smirnova, N.P., Linnik, O.P.. 2017. Nonporous platinum doped titania films: synthesis, optical and photocatalytic characteristics. *Chemistry, Physics and Technology of Surface*. 8 (4): 369-375.

Inoue, T., Fujishima, A., Konishi, S. and Honda, K. 1979. Photoelectrocatalytic reduction of carbon dioxide in aqueous suspensions of semiconductor powders. *Nature*, 277: 637–638.

Iwashina, K., Iwase, A., Ng, Y. H., Amal, R. and Kudo A. 2015. Z-schematic water splitting into H2 and O2 using metal sulfide as a hydrogen-evolving photocatalyst and reduced graphene oxide as a solid-state electron mediator. *J. Am. Chem. Soc.*, 137: 604–607.

Johns, JE, Hersam, MC. 2013. Atomic covalent functionalization of graphene. *Acc Chem Res*, 46:77–86.

Jun, Y., Lee, E.Z., Wang, X., Hong, W.H., Stucky, G.D. And Thomas, A., 2013. From Melamine-Cyanuric Acid Supramolecular Aggregates to Carbon Nitride Hollow Spheres. *Advanced Functional Materials,* 23(29): 3661-3667.

Jun, Y., Hong, W.H., Antonietti, M. And Thomas, A., 2009. Mesoporous, 2D Hexagonal Carbon Nitride and Titanium Nitride/Carbon Composites. *Advanced Materials,* 21(42): 4270-4274.

Khan M.M., Pradhan, D. and Sohn, Y. (eds). 2017. *Nanocomposites for Visible Light-induced Photocatalysis*, Springer Series on Polymer and Composite Material. Chapter 2: Basic Principles, Mechanism and Challenges of Photocatalysis; Chapter 7: Polymeric Nanocomposites for Visible-Light-Induced Photocatalysis. Chapter 9: Nanocomposites of g-C3N4 with Carbonaceous p-conjugated/Polymeric Materials TowardsVisible Light-Induced Photocatalysis. Switzerland: Springer International Publishing AG.

Khan, M.M., Adil, S.F. and Al-Mayouf, A. 2015. Metal oxides as photocatalysts. *J Saudi Chem Soc,* 19 (5): 462 – 464.

Kisch, H. 2013. Semiconductor Photocatalysis – Mechanistic and Synthetic Aspects. *Angew Chem Int Ed*, 52: 812 – 847.

Kruk, M., Dufour, B., Celer, E.B., Kowalewski, T., Jaroniec, M. And Matyjaszewski, K., 2005. Synthesis of Mesoporous Carbons Using Ordered and Disordered Mesoporous Silica Templates and Polyacrylonitrile as Carbon Precursor. *The journal of physical chemistry. B,* 109(19): 9216-9225.

Leary, R., Westwood, A. 2011. Carbonaceous nanomaterials for the enhancement of TiO2. *Photocat Carbon,* 49: 741–77.

Lee, J.S., Wang, X., Luo, H. And Dai, S., 2010. Fluidic Carbon Precursors for Formation of Functional Carbon under Ambient Pressure Based on Ionic Liquids. *Advanced materials* (Deerfield Beach, Fla.), 22(9), pp. 1004-1007.

Lee, J.S., Wang, X., Luo, H., Baker, G.A. And Dai, S., 2009. Facile Ionothermal Synthesis of Microporous and Mesoporous Carbons from Task Specific Ionic Liquids. *Journal of the American Chemical Society*, 131(13): 4596-4597.

Li, Q, Guo, B, Yu, J, Ran, J, Zhang, B, Yan, H, Gong, JR. 2011. Highly efficient visible-light-driven photocatalytic hydrogen production of CdS-cluster-decorated graphene nanosheets. *J AmChem Soc* 133(28):10878–10884.

Liang, Q., Jiang, G. Y., Zhao, Z., Li, Z. Y., and MacLachlan, M. J. 2015. CdS-decorated triptycene-based polymer: durable photocatalysts for hydrogen production under visible-light irradiation. *Catal. Sci. Technol*., 5: 3368–3374.

Liang, Z, Xu, P, Wang, W, Zhang, D, Xiao, S, Li, X, Li, G. 2015b. C60-decorated CdS/TiO2 mesoporous architectures with enhanced photostability and photocatalytic activity for H2 evolution. *ACSAppl Mater Interfaces*, 7(8):4533–4540

Liebig, J. V. 1834. Uber einige Stickstoff - Verbindungen. *Ann Pharm*,10, 10.

Linnik, O., Smirnova, N., Korduban, O., Eremenko, A. 2013. Gold nanoparticles into Ti1xZnxO2 films: Synthesis, structure and application. *Materials Chemistry and Physics* 142 (2013): 318-324.

Liu, H, Chen, Z, Wang, Y. 2016a. Plasmonic Ag coated BiOBr 0.2I0.8 nanosheets grown on graphenewith excellent visible-light photocatalytic activity. *J Photochem Photobiol A*, 326:30–40.

Liu, Q, Chen, T, Guo, Y, Zhang, Z, Fang, X. 2016b. Ultrathin g-C3N4nanosheets coupled withcarbon nanodots as 2D/0D composites for efficient photocatalytic H2evolution. *Appl Catal B*, 193: 248–258.

Liu, S, Li, D, Sun, H, Ang, HM, Tadé, MO, Wang, S. 2016c. Oxygen functional groups in graphiticcarbon nitride for enhanced photocatalysis. *J Colloid Interface Sci*, 468: 176–182.

Liu, Q., Zhou, Y., Kou, J. H., Chen, X. Y., Tian, Z. P., Gao, J., Yan, S. C., and Zou, Z. G.. 2010. High-yield synthesis of ultralong and ultrathin Zn2GeO4 nanoribbons toward improved photocatalytic reduction of CO2 into renewable hydrocarbon fuel. *J. Am. Chem. Soc*. 132(41), 14385–14387.

Low, J., B. Cheng, J. Yu and M. Jaroniec. 2015. Graphene-Based Photocatalysts for CO2 Reduction to Solar Fuel . *Energy Storage Materials*, 3: 24–35.

Lu, P., Qiao, B., Lu, N., Hyun, D.Ch., Wang, J., Kim, M.J., Liu, J., Xia, Y. 2015. Photochemical Deposition of Highly Dispersed Pt Nanoparticles on Porous CeO_2 Nanofibers for the Water-Gas Shift Reaction. *Adv Fun Mat*, 25(26): 4153-4162.

Luo, B., G. Liu and L. Z. Wang. 2016. Recent advances in 2D materials for photocatalysis. *Nanoscale,* 8: 6904–6920.

Malato, S., Fernández-Ibáñez, P., Maldonado, M.I., Blanco, J., Gernjak, W. 2009. Decontamination and disinfection of water by solar photocatalysis: recent overviewand trends. *Catal Today*, 147(1): 1–59.

Martin, D.J. 2015. *Investigation into High Efficiency Visible Light Photocatalysts for Water Reduction and Oxidation*. Doctoral Thesis. Switzerland: Springer Theses. DOI 10.1007/978-3-319-18488-3_1

Matsumoto, Y, Miura, Y, Takata, S. 2016. Thickness-dependentflat band potential of anataseTiO2(001) epitaxialfilms on Nb:SrTiO3(001) investigated by UHV-electrochemistry approach. *J Phys Chem C,* 120(3): 1472–1477.

Mendive, C.B., Hansmann, D., Bredow, T., Bahnemann, D. 2011. New insights into the mechanism ofTiO_2 photocatalysis: thermal processes beyond the electron-hole creation. *J Phys Chem C*, 115: 19676−19685.

Neppolian, B., Choi, H.S., Sakthivel, S., Arabindoo, B., Murugesan, V. 2002. Solar light induced and TiO2 assisted degradation of textile dye reactive blue 4. *Chemosphere,* 46: 1173–1181.

Oceanoptics.com. 2019. *Example Setups: Modular Spectroscopy Setups for Absorbance, Reflection, Emission & More.* [Accessed 20th of October] Available at: https://oceanoptics.com/knowledge-support/example-setups/

Ong, W.J., L.L. Tan, Y. H. Ng, S.-T. Yong and S.-P. Chai. 2016. Graphitic Carbon Nitride (g-C3N4)-Based Photocatalysts for Artificial Photosynthesis and Environmental Remediation: Are We a Step Closer To Achieving Sustainability? *Chem. Rev*., 116: 7159–7329.

Park, H., hul Lee, Y.C., Choi, B.G., Choi, Y.S., Yang, J.W., Hong, W.H. 2010. Energy transfer inionic-liquid-functionalized inorganic nanorods for highly efficient photocatalytic applications. *Small*, 6 (2): 290–295.

Pawinrat P., O. Mekasuwandumrong and J. Panpranot. 2009. Synthesis of Au-ZnO and Pt-ZnO Nanocomposites by One-Step Flame Spray Pyrolysis and Its Application for Photocatalytic Degradation of Dyes. *Catal. Commun*., 10, 1380–1385.

Quintana, M., Ke, X., Van Tendeloo, G., Meneghetti, M., Bittencourt, C., Prato, M. 2010. Light-Induced Selective Deposition of Au Nanoparticles on Single-Wall Carbon Nanotubes. *ACS Nano*, 4, 10: 6105-6113.

Rajeshwar, K., Osugi, M.E., Chanmanee, W., Chenthamarakshan, C.R., Zanoni, M., Kajitvichyanukul, P., Krishnan-Ayer, R. 2008. Heterogeneous photocatalytic treatment of organic dyes in air andaqueous media. *J Photochem Photobiol C*, 9 (4): 171–192.

Rehman S., R. Ullah, A. M. Butt and N. D. Gohar. 2009. Strategies of making TiO2 and ZnO visible light active. *J. Hazard.Mater*., 170, 560–569.

Reza, K.M., Kurny, A.S., Gulshan, F. 2015. Parameters affecting the photocatalytic degradation ofdyes using TiO2: a review. *Appl Water Sci*. doi:10.1007/s13201-015-0367-y

Rusina, O., Macyk, W. and Kisch, H. 2005. Photoelectrochemical Properties of a Dinitrogen-Fixing Iron Titanate Thin Film. *J. Phys. Chem. B*, 109: 10858-10862.

Serp, P, Corrias, M, Kalck, P. 2003. Carbon nanotubes and nanofibers in catalysis. *Appl Catal A*, 253(2): 337–358.

Shalom, M., Inal, S., Fettkenhauer, C., Neher, D. And Antonietti, M., 2013. Improving Carbon Nitride Photocatalysis by Supramolecular Preorganization of Monomers. *Journal of the American Chemical Society*, 135(19): 7118-7121.

Shi, L, Wang, T, Zhang, H, Chang, K, Meng, X, Liu, H, Ye, J. 2015. An amine-functionalized iron(III) metal–organic framework as efficient visible-light photocatalyst for Cr(VI) reduction. *Adv Sci* 2(3)

Sun, L., Yang, M., Huang, J., Yu, D., Hong, W., Chen, X. 2016 , Freestanding Graphitic Carbon Nitride Photonic Crystals for Enhanced Photocatalysis. *Adv Fun Mat*, 26, 4943 – 4950

Tajima, T., Sakata, W., Wada, T., Tsutsui, A., Nishimoto, S., Miyake, M., Takaguchi, Y. 2011. Photosensitized hydrogen evolution from water using a single-walled carbon nanotube/fullerodendron/SiO2 coaxial nanohybrid. *Mater Adv*, 23 (48): 5750–5754.

Tang J. W., Z. G. Zou and J. H. Ye. 2004. Efficient photocatalytic decomposition of organic contaminants over CaBi2O4 under visible-light irradiation. *Angew. Chem., Int. Ed*., 43, 4463–4466.

Tang J. W., Z. G. Zou and J. H. Ye. 2003. Photophysical and Photocatalytic Properties of $AgInW_2O_8$. *J. Phys. Chem. B*, 107, 14265–14269.

Tian, Y. and Tatsuma, T. 2005. Mechanisms and Applications of Plasmon-Induced Charge Separation at TiO2 Films Loaded with Gold Nanoparticles. *J Am Chem Soc*, 127: 7632–7637.

Tryba, B. (2008) Increase of the photocatalytic activity of TiO by carbon and iron modifications. *Int J Photoenergy* 2008.

Uddin, M. T., Nicolas, Y., Olivier, C., Toupance, T., Servant, L., Muller, M. M., Kleebe, H. J., Ziegler, J. and Jaegermann, W. 2012. Nanostructured SnO2-ZnO heterojunction photocatalysts showing enhanced photocatalytic activity for the degradation of organic dyes. *Inorg. Chem*., 51, 7764–7773.

Ullah R.and J. Dutta. 2008. Photocatalytic degradation of organic dyes with manganese-doped ZnO nanoparticles. *J. Hazard. Mater*., 156, 194–200.

van de Krol, R. and Grätzel, M. (eds.). 2012. Photoelectrochemical Hydrogen Production, *Electronic Materials: Science & Technology 102*. Switzerland: Springer Science+Business Media. DOI 10.1007/978-1-4614-1380-6_1.

Van Dijken, A., Vanmaekelbergh, D. and Meijerink, A. 1997. Size selective photoetching of nanocrystalline CdS particles. *Chem.Phys. Lett.*, ,269: 494–499.

Wang, B., Li, Ch., Cui, H., Zhang, J., Zhai, J., Li, Q. 2013. Fabrication and enhanced visible-light photocatalytic activity of Pt-deposited TiO_2 hollow nanospheres. *Chem Eng J*, 223: 592-603.

Wang, X., Blechert, S. And Antonietti, M., 2012. Polymeric Graphitic Carbon Nitride for Heterogeneous Photocatalysis. *ACS Catalysis*, 2 (8): 1596-1606.

Wang, Y., Wang, X. and Antonietti, M. 2012. Polymeric Graphitic Carbon Nitride as a Heterogeneous Organocatalyst: From Photochemistry to Multipurpose Catalysis to Sustainable Chemistry. *Angew Chem Int Ed*, 51 (1): 68-89.

Wang, X, Maeda, K., Thomas, A., Takanabe, K., Gang Xin, G., Carlsson, J.M., Domen, K., Antonietti, M. 2009. A metal-free polymeric photocatalyst for hydrogen production from water under visiblelight. *Nat Mater*, 8: 76–80.

Xing, M., Li, X., Zhang, J. 2014. Synergistic effect on the visible light activity of Ti3+doped TiO2 nanorods/boron doped graphene composite. *Sci Rep* 4

Xu, Y., Kraft, M. and Xu, R.. 2016. Metal-free carbonaceous electrocatalysts and photocatalysts for water splitting. *Chem. Soc. Rev*., 45: 3039–3052.

Yamagata, S., Nakabayashi, S., Sancier, K. M. and Fujishima, A. 1988. Photocatalytic Oxidation of Alcohols on TiO2. *Bull Chem Soc Jpn*, 61: 3429–3434.

Yamakoshi, Y., Umezawa, N., Ryu, A., Arakane, K., Miyata, N., Goda, Y., Masumizu, T., Nagano, T. 2003. Active oxygen species generated from photoexcited fullerene (C60) as potential medicines: O2-*versus1O2. *J Am Chem Soc*, 125(42): 12803–12309.

Yang, M.Q., Zhang, N., Xu, Y.J. 2013. Synthesis of fullerene–, carbon nanotube–, and graphene–TiO_2 nanocomposite photocatalysts for selective oxidation: a comparative study. *ACS Appl Mater Interfaces*, 5 (3): 1156–1164.

Yang, Z., Zhang, Y. And Schnepp, Z., 2015. Soft and hard templating of graphitic carbon nitride. *J of Mater Chem A*, 3(27), pp. 1481-1492.

Yao, Z., Wang, L., Zhang, Y., Yu, Z., Jiang, Z. 2014. Carbon nanotube modified Zn0.83Cd0.17S nanocomposite photocatalyst and its hydrogen production under visible-light. *Int J Hydrogen Energy*, 39 (28): 15380–15386.

Yu, Z., Yin, B. S., Qu, F. Y. and Wu, X. 2014. Synthesis of self-assembled CdS nanospheres and their photocatalytic activities by photodegradation of organic dye molecules. *Chem Eng J*, 258: 203–209.

Zhang, P., Zhang, J. and Dai, S., 2017. Mesoporous Carbon Materials with Functional Compositions. *Chemistry – A European Journal*, 23 (9): 1986-1998.

Zhang, L., Bao, Z., Yu, X., Dai, P., Zhu, J., Wu, M., Li, G., Liu, X., Sun, Z., Chen, C. 2016a. Rational design of a-Fe2O3/reduced graphene oxide composites: rapid detection and effective removal oforganic pollutants. *ACS Appl Mater Interfaces*, 8(10): 6431–6438.

Zhang, X., Qi Wang, Q., Zou, L.H., You, J.W. 2016b. Facile fabrication of titanium dioxide/fullerenenanocomposite and its enhanced visible photocatalytic activity. *J Colloid Interface Sci*, 466: 56–61.

Zhang, J., Guo, F. and Wang, X., 2013. An Optimized and General Synthetic Strategy for Fabrication of Polymeric Carbon Nitride Nanoarchitectures. *Advanced Functional Materials*, 23(23), pp. 3008-3014.

Zhang, Z., Yates, J.T. Jr. 2012. Band bending in semiconductors: chemical and physical consequences at surfaces and interfaces. *Chem Rev*, 112: 5520–5551.

Zhang, H., Lv, X., Li, Y., Wang, Y., Li, J. 2010. P25-graphene composite as a high performance photocatalyst. *ACS Nano*, 4 (1): 380–386.

Zhao, H, Chen, S, Quan, X, Yu, H, Zhao, H. 2016. Integration of microfiltration and visible-light-driven photocatalysis on g-C_3N_4 nanosheet/reduced graphene oxide membrane for enhanced water treatment. *Appl Catal B*, 104: 134–140.

Zheng, Y., Lin, L. H., Wang, B.and Wang, X. C. 2015. Graphitic Carbon Nitride Polymers toward Sustainable Photoredox Catalysis. *Angew.Chem., Int. Ed.*, 53, 12868–12884.

Zheng, Y., Liu, J., Liang, J., Jaroniec, M.and Qiao, S. Z.. 2012. Graphitic carbon nitride materials: controllable synthesis and applications in fuel cells and photocatalysis. *EnergyEnviron. Sci.*, 2012,5, 6717–6731

Zhou, Y., Zhang, L., Huang, W., Kong, Q., Fan, X., Wang, M. And Shi, J., 2016. N-doped graphitic carbon-incorporated g-C3N4for remarkablyenhanced photocatalytic H2evolution under visible light. *Carbon*, 99: 111-117.

Zhou, L., Zhang, H., Sun, H., Liu, Sh., Tade, O.M., Wang, Sh. and Jin, W. 2016. Recent advances in non-metal modification of graphitic carbon nitride for photocatalysis: a historic view. *Catal Sci Technol*, 6: 7002.

Zhu, J. J., P. Xiao, H. L. Li and S. A. C. Carabineiro. Graphitic Carbon Nitride: Synthesis, Properties, and Applications in Catalysis, *ACS Appl. Mater. Interfaces*, 2014,6, 16449–16465.